Medical Image Analysis 17 (2013) 556–572

Contents lists available at SciVerse ScienceDirect

Medical Image Analysis

journal homepage: www.elsevier.com/locate/media

Continuous diffusion signal, EAP and ODF estimation via Compressive Sensing in diffusion MRI

Sylvain. L Merlet *, Rachid Deriche

Athena Project-Team, INRIA Sophia Antipolis – Méditerranée, France

ARTICLE INFO

Article history:
Received 29 May 2012
Received in revised form 19 February 2013
Accepted 26 February 2013
Available online 20 March 2013

Keywords:
Compressive Sensing
MRI
Diffusion MRI
Orientation Distribution Function
Ensemble Average Propagator
White matter

ABSTRACT

In this paper, we exploit the ability of Compressed Sensing (CS) to recover the whole 3D Diffusion MRI (dMRI) signal from a limited number of samples while efficiently recovering important diffusion features such as the Ensemble Average Propagator (EAP) and the Orientation Distribution Function (ODF). Some attempts to use CS in estimating diffusion signals have been done recently. However, this was mainly an experimental insight of CS capabilities in dMRI and the CS theory has not been fully exploited. In this work, we also propose to study the impact of the sparsity, the incoherence and the RIP property on the reconstruction of diffusion signals. We show that an efficient use of the CS theory enables to drastically reduce the number of measurements commonly used in dMRI acquisitions. Only 20–30 measurements, optimally spread on several *b*-value shells, are shown to be necessary, which is less than previous attempts to recover the diffusion signal using CS. This opens an attractive perspective to measure the diffusion signals in white matter within a reduced acquisition time and shows that CS holds great promise and opens new and exciting perspectives in diffusion MRI (dMRI).

1. Introduction

Diffusion MRI (dMRI) is a recent Magnetic Resonance Imaging technique introduced by (Le Bihan and Breton, 1985; Merboldt et al., 1985; Taylor and Bushell, 1985). Since the first acquisitions of diffusion-weighted images (DWIs) in vivo, dMRI has become an established research tool for the investigation of tissue structure and orientation.

In 1965, (Stejskal and Tanner, 1965) introduced the pulsed gradient spin-echo (PGSE) sequence. It allows the quantification of the diffusion by estimating the displacement of particles from the phase change that occurs during the acquisition process. When the gradient pulses are sufficiently short, it's well known that the measured signal $E(\mathbf{q})$, after normalization, is written as the Fourier transform of the Ensemble Average Propagator (EAP) $P(\mathbf{R})$

$$E(\mathbf{q}) = \int_{\mathbf{R}\in\mathcal{R}^3} P(\mathbf{R}) \exp(-2\pi i \mathbf{q}\cdot\mathbf{R}) d\mathbf{R}, \quad (1)$$

where $\mathbf{q}$ and $\mathbf{R}$ are both 3D-vectors that respectively represent the effective gradient direction and the displacement direction. We can decompose them as $\mathbf{q} = q\mathbf{u}$ and $\mathbf{R} = R\mathbf{r}$, where $\mathbf{u}$ and $\mathbf{r}$ are 3D unit vectors.

Using dMRI to infer the EAP requires the acquisition of many diffusion images sensitized to different orientations in the sampling space. The number of diffusion weighted images (DWI) required depends on how the diffusion is modeled. For instance, the well known Diffusion Tensor (DT) model (Basser et al., 1994b,a) assumes the EAP is Gaussian and requires at least 6 DWIs plus an additional unweighted image. However, the Gaussian assumption, in Diffusion Tensor Imaging (DTI), is an over-simplification of the diffusion of water molecules in the brain and, thus, has some limitations for voxels in which there are more complicated internal structures. Therefore, it is of utmost importance to develop techniques that go beyond the limitations of DTI. For this purpose, High Angular Resolution Diffusion Imaging (HARDI) has been proposed to measure the diffusion of water molecules along more directions than DTI does. Among HARDI techniques, there is Q-Ball Imaging (QBI) (Tuch, 2004; Anderson, 2005; Descoteaux et al., 2007), which estimates the Orientation Distribution Function (ODF) from measurements taken at same radii. The ODF gives the probability that a water molecule diffuses in a given direction. Both numerical (Tuch, 2004) and analytical (Descoteaux et al., 2007; Anderson, 2005) solutions have been proposed for QBI. At first, the ODF was defined as the integration of the EAP over its radius (Tuch, 2004). Only recently was considered the correct mathematical formulation (Aganj et al., 2010; Tristn-Vega et al., 2009), which results in the normalized ODF expression. (Wedeen et al., 2005; Aganj et al., 2010; Tristn-Vega et al., 2009) express the ODF $\Upsilon(\mathbf{r})$ as the integration of the EAP over a solid angle, i.e.

$$\Upsilon(\mathbf{r}) = \int_0^\infty P(R.\mathbf{r}) R^2 \, dR. \quad (2)$$

* Corresponding author.
E-mail address: sylvain.merlet@inria.fr (S. Merlet).

1361-8415/$ - see front matter © 2013 Elsevier B.V. All rights reserved.
http://dx.doi.org/10.1016/j.media.2013.02.010

However, the ODF only captures angular information of the diffusion process. Another HARDI technique has been proposed in (Jian et al., 2007), where the authors characterize the diffusion signal by a continuous mixture of Gaussian, resulting to a Wishart distribution. (Jian et al., 2007) shows improvements over the classical DTI technique and present an estimation scheme for the fiber orientation and EAP. Considering basics of dMRI, another technique known as Diffusion Spectrum Imaging (DSI) appeared (Wedeen et al., 2005). In DSI, we obtain the EAP $P(\mathbf{R})$ by directly taking the inverse Fourier transform of the normalized signal $E(\mathbf{q})$ measured in the q-space (see Eq. (1)). It aims to reconstruct the EAP in a numerical way without any prior knowledge. This results in estimating the EAP in a more accurate fashion than any other methods.

However, many measurements and a long acquisition time are necessary to obtain high-resolution EAP. Therefore, it's clear that there is a strong need for new techniques to estimate the whole EAP with fewer measurements. To this end, multiple shells HARDI methods have been used (zarslan et al., 2006; Assemlal et al., 2009; Ozarslan et al., 2009; Cheng et al., 2010b; Descoteaux et al., 2011; Wu and Alexander, 2007; Hosseinbor et al., 2011). They consist in acquiring the signal following multiple shells schemes and then, modeling it with an adequate basis. These techniques aim to catch both radial and angular information about the water diffusion process. However, an increase of the number of measurements is expected over methods as DTI or QBI. An important problem is to accurately estimate the diffusion signal and the underlying EAP with a small number of samples. A first answer has been given while using suitable bases as the Spherical Polar Fourier (SPF) basis (Assemlal et al., 2009), the SPF dual (SPFdual) basis (Merlet et al., 2011b), the Solid Harmonic (SoH) basis (Descoteaux et al., 2011) or the SHORE basis (Ozarslan et al., 2009). We give a complementary solution by using a new acquisition and reconstruction technique called Compressive Sensing (CS).

CS aims to accurately reconstruct signals from under sampled measurements (Donoho, 2006; Candes and Wakin, 2008). This method relies on several properties: The signal to recover admits a sparse representation; the basis, in which the signal is modeled, is sufficiently incoherent; a robust acquisition protocol and an efficient reconstruction scheme is used. CS has been proven useful in recovering Magnetic Resonance (MR) images by significantly undersampling their k-spaces (Lustig et al., 2007; Guo and Yin, 2010, 2008, 2009). The application of CS in diffusion MRI is recent and can be separated in two categories: discrete CS recovering and continuous CS recovering. Discrete CS recovering has been used to accelerate the DSI technique (Merlet and Deriche, 2010; Saint-Amant and Descoteaux, 2011; Menzel et al., 2011), by exploiting the Fourier relation between the diffusion signal and the EAP. However, the so called "CS-DSI" problem consists in reconstructing a discrete version of the EAP and diffusion features have to be computed numerically.

Continuous CS recovering consists in modeling a signal with a continuous framework from few measurements via a CS reconstruction. A continuous signal modeling is advantageous because it is not acquisition dependent and enables data interpolation and extrapolation. Some works have been published toward this (Michailovich and Rathi, 2010; Rathi et al., 2011; Cheng et al., 2011b; Merlet et al., 2011b; Tristán-Vega and Westin, 2011). In (Michailovich and Rathi, 2010; Tristán-Vega and Westin, 2011), the authors work with measurements taken at same radii and only estimate the ODF. (Rathi et al., 2011) generalizes the single shell spherical ridgelets basis of (Michailovich and Rathi, 2010) to a multiple shells framework for a sparse and continuous representation of the diffusion signal. In (Rathi et al., 2011), a total number of 64 measurements are used to well estimate the diffusion signal. However, it does not provide any analytical formula to estimate diffusion features. (Cheng et al., 2011b; Merlet et al., 2011b) consider a CS reconstruction combined with a continuous representation of the diffusion signal and available closed formulae to estimate the EAP and the ODF. (Merlet et al., 2011b) is about CS recovering in SPFdual basis with 80 measurements and (Cheng et al., 2011b) is about CS recovering in SPF basis from a minimum number of 60 measurements. These two papers give a first experimental insight of CS capabilities in dMRI, where analytical formulae are available to estimate the EAP and the ODF.

It is also worthwhile to note that very recent works started to handle the learning of dictionaries from a training data set (Ye et al., 2012; Merlet et al., 2012; Gramfort et al., 2012; Bilgic et al., 2012). These techniques lead to very sparse representations of diffusion signals and are worth to be minutely investigated. The analysis done in this paper considers predefined sets of functions that form orthonormal bases commonly used in the dMRI field. The question of which basis would result in the most efficient description of diffusion signals is not addressed here and is outside the scope of the paper.

In this paper, we investigate the Compressive Sensing technique in order to accurately and continuously estimate the full 3D diffusion phenomenon as well as some of its features with a very small number of samples. More precisely, we show that only 20/30 measurements are necessary to well estimate the diffusion signal. It is nearly three times less than previous studies encountered in (Merlet et al., 2011b; Cheng et al., 2011b; Rathi et al., 2011). This significant improvement over these previous works is due to a correct use and consideration of every point of the CS theory. Then, we demonstrate that it is worth using CS recovery, when CS requirements are fulfilled and we also demonstrate how to take advantage of this technique. Before starting with the central point of this paper, i.e. the CS technique, we describe, in the first section, four bases used to model the diffusion signal. Our approach consider common and continuous representations of the diffusion signal, which enable to obtain various diffusion features such the EAP and the ODF (as in (Merlet et al., 2011b; Cheng et al., 2011b)). Then, we give, in the second part (Section 3), a complete description of the CS properties. In Sections 3.1 and 3.2 respectively, we study the incoherence and sparse properties of the bases described in Section 1. Section 3.3 describes the reconstruction scheme used in CS recovery and the related theoretical results. We also, handle in Section 3.3, the acquisition point by describing some theoretical tools to validate sampling protocols, i.e. a partial evaluation of the Restricted Isometry Property (RIP). These points are studied both in a theoretical and experimental way. In the last part, we present some experimental results confronting CS recovery and state of the art recovery. In this experimental part, we begin with synthetic data and focus our attention on several points: (1) the sampling protocol (Section 4.1), where a powerful technique is described to build robust sampling schemes and (2) the quality of reconstruction on noisy synthetic data (Section 4.2). Especially in Section 4.2, we demonstrate how efficient is the CS recovery in reconstructing the diffusion signal and the ODF. These synthetic experiments also enable to compare our CS-based EAP recovery with the EAP obtained via the DSI technique. Then, we give in Sections 4.3 and 4.4 some results, respectively on real monkey brain data and phantom data.

From these experiments, we finally show that CS enables to accurately handle the whole diffusion process with a smaller number of samples than state-of-the-art methods (~20/30 measurements), while modeling the diffusion signal in one of the bases described in the following.

2. Bases for diffusion signal modeling

In this section we describe four bases used to model the diffusion signal, known as

Table 1
$\Psi_{n\ell m}(R\mathbf{r})$ coefficients for the EAP closed formulae (see Eq. (8)). For SoH basis: $n!! = (n)(n-2)\cdots(4)(2)$, $J_n(x)$ is the Bessel function of order n, Z a normalization constant and q_{max} the maximum q-value used during the acquisition.

SPF	$\Phi_{n\ell m}^{(\text{SPFdual})}(R\mathbf{r})$ (Cheng et al., 2010b)
SPFdual	$\Phi_{n\ell m}^{(\text{SPF})}(R\mathbf{r})$ (Merlet et al., 2011b)
SoH	$\frac{1}{Z}\left[\frac{(-1)^{l/2}}{R^{3/2}}\left[\frac{2^l R^{l-1/2}\pi^{l-1}}{(2l-1)!!} - \frac{J_{l-1/2}(2\pi q_{max}R)}{q_{max}^{l-1/2}}\right]c_{lm} + (-1)^{l/2} q_{max}^{l+3/2} R^{-3/2} J_{l+3/2}(2\pi q_{max}R) d_{lm}\right] Y_\ell^m(\mathbf{r})$ (Descoteaux et al., 2011)
SHORE	$(-1)^{n-l/2}\left[\frac{2(4\pi^2\zeta)^{3/2}(n-\ell)!}{\Gamma(n+3/2)}\right]^{1/2}\left(4\pi^2\zeta R^2\right)^{l/2}\exp\left(-2\pi^2\zeta R^2\right)L_{n-\ell}^{l+1/2}\left(4\pi^2\zeta R^2\right)Y_\ell^m(\mathbf{r})$ (Cheng et al., 2011a)

- The Spherical Polar Fourier (SPF) basis (Assemlal et al., 2009; Cheng et al., 2010b)
- The SPF dual (SPFdual) basis (Merlet et al., 2011b) Appendix B.
- The Solid Harmonic (SoH) basis, which is part of the DPI method (Descoteaux et al., 2011).
- The SHORE basis (Ozarslan et al., 2009; Cheng et al., 2011a) Appendix C.

We consider these bases because they are the most commonly used in dMRI for a continuous modeling of the diffusion signal. Furthermore, closed formulae for some diffusion features, such that the EAP and the ODF, have been analytically derived in (Descoteaux et al., 2011; Cheng et al., 2010b; Cheng et al., 2010a; Cheng et al., 2011a) and Appendices B, C.

Our presentation is structured as follows: We first give the analytical formulation for the bases functions (Section 2.1) and, then, give the closed formulae for the EAP and ODF (Section 2.2).

Notations: Before exploring this topic any further, we need to set some notations. We call $E(\mathbf{q}) = S(\mathbf{q})/S_0$ the normalized diffusion signal with $S(\mathbf{q})$ the diffusion signal acquired at $\mathbf{q}$ in the q-space and S_0 the signal without any gradient applied. $\mathbf{q}$ is a 3D-vector, which can be decomposed in $\mathbf{q} = q\mathbf{u}$, where $\mathbf{u}$ is a 3D unit vector. $P(\mathbf{R})$ is the EAP at the 3D space location $\mathbf{R} = R\mathbf{r}$, with $\mathbf{r}$ is a 3D unit vector.

2.1. Diffusion signal modeling

We represent $E(q\mathbf{u})$ as a truncated linear combination of $\Phi_{n\ell m}(q\mathbf{u})$ with n the radial order, ℓ and m the angular order and degree,

$$E(q\mathbf{u}) = \sum_{n=0}^{N}\sum_{\ell=0}^{L}\sum_{m=-\ell}^{\ell} c_{n\ell m}\Phi_{n\ell m}(q\mathbf{u}) \tag{3}$$

where the $c_{n\ell m} = \langle E, \Phi_{n\ell m}\rangle$ are the transform coefficients.

2.1.1. Diffusion signal modeling in the SPF basis

The orthonormal Spherical Polar Fourier basis was used by (Assemlal et al., 2009), in order to describe the diffusion signal E. (Assemlal et al., 2009) reports that the SPF basis is appropriate to sparsely represent multiple configurations of the water diffusion including isotropy and crossing fibers aspects as well as the multiple compartments profile. (Assemlal et al., 2009) describes the SPF basis function $\Phi_{n\ell m}^{(\text{SPF})}(q\mathbf{u})$ as

$$\Phi_{n\ell m}^{(\text{SPF})}(q\mathbf{u}) = \left[\frac{2n!}{\zeta^{3/2}\Gamma(n+3/2)}\right]^{1/2} exp\left(\frac{-q^2}{2\zeta}\right)L_n^{1/2}\left(\frac{q^2}{\zeta}\right)Y_\ell^m(\mathbf{u}), \tag{4}$$

where ζ is a scale factor, $L_n^{(1/2)}$ is the generalized Laguerre polynomial $L_n^{(\alpha)}$, of order n with $\alpha = 1/2$, and $Y_\ell^m(\mathbf{u})$ is the Spherical Harmonic (SH) function of order $\ell$and degree m. Note that we use the real and symmetric version of the Spherical Harmonic basis, i.e. we consider only the SH of even degree.

2.1.2. Diffusion signal modeling in the SPFdual basis

Here, the SPF basis is not used to model the diffusion signal but the EAP. Then, (Merlet et al., 2011b) derives a dual basis to model E. This formulation was first used in a reconstruction in (Merlet et al., 2011b). (Merlet et al., 2011b) expresses the SPFdual basis function $\Phi_{n\ell m}^{(\text{SPFdual})}$ as

$$\Phi_{n\ell m}^{(\text{SPFdual})}(q\mathbf{u}) = 4(-1)^{\ell/2}\frac{\zeta^{\ell/2+3/2}\pi^{\ell+3/2}q^\ell}{\Gamma(l+3/2)}\gamma(\zeta,q)Y_\ell^m(\mathbf{u}),$$
$$\text{with}\quad \gamma(\zeta,q) = \left[\frac{2^\ell n!}{\zeta^{\frac{3}{2}}\Gamma(n+\frac{3}{2})}\right]^{\frac{1}{2}}\sum_{k=0}^{n}\frac{(-1)^k}{k!}\binom{n+\frac{1}{2}}{n-k}2^k \tag{5}$$
$$\Gamma\left(\frac{\ell}{2}+k+\frac{3}{2}\right){}_1F_1\left(\frac{2k+l+3}{2}, l+\frac{3}{2}, -2(\pi q)^2\zeta\right),$$

where ${}_1F_1$ is the confluent hypergeometric function and Γ the Gamma function. Note that $\Phi_{n\ell m}^{(\text{SPFdual})}$ and $\Phi_{n\ell m}^{(\text{SPF})}$ (in Eq. (4)) are related by a Fourier transform.

2.1.3. Diffusion signal modeling in the SHORE basis

The SHORE basis has been introduced by (Ozarslan et al., 2009) but the basis was only orthogonal. (Cheng et al., 2010b) proposed a new formulation where the basis functions have a l_2 norm equal to one. This orthonormal basis is a generalization of the SPF basis and $\Phi_{n\ell m}^{(\text{SHORE})}$ is expressed as,

$$\Phi_{n\ell m}^{(\text{SHORE})}(q\mathbf{u}) = \left[\frac{2(n-\ell)!}{\zeta^{3/2}\Gamma(n+3/2)}\right]^{1/2}\left(\frac{q^2}{\zeta}\right)^{l/2}$$
$$\times \exp\left(\frac{-q^2}{2\zeta}\right)L_{n-\ell}^{l+1/2}\left(\frac{q^2}{\zeta}\right)Y_\ell^m(\mathbf{u}). \tag{6}$$

Note that, because the Laguerre polynomial order ($n-\ell$ in Eq. (6)) must be positive, the angular order ℓ depends on the radial order n, such that $n \geqslant \ell$. Then, the angular order $\ell$is bounded by n.

2.1.4. Diffusion signal modeling in the SoH basis

(Descoteaux et al., 2011) considers the total 3D solution to the Laplace equation in spherical coordinates, i.e. the angular and radial part. It results in the Solid Harmonic (SoH) basis. In this framework, the diffusion E is approximated by two series of SH coefficients $c_{\ell m}$ and $d_{\ell m}$, i.e. the radial order is fixed to 2. We have

$$E(q\mathbf{u}) = \sum_{\ell=0}^{L}\sum_{m=-\ell}^{\ell}\underbrace{\left[\frac{c_{\ell m}}{q^{l+1}} + d_{\ell m}q^l\right]}_{radialpart}Y_\ell^m(\mathbf{u}) = \sum_{\ell=0}^{L}\sum_{m=-\ell}^{\ell}\Phi_{\ell m}^{(\text{SoH})}(q\mathbf{u}). \tag{7}$$

2.2. EAP and ODF modeling

As described in Eq. (1), the EAP P and the diffusion signal E are related by a Fourier transform. Following this relation, we can obtain a closed formula to estimate P from E as follows:

$$P(R\mathbf{r}) = \sum_{n=0}^{N}\sum_{\ell=0}^{L}\sum_{m=-\ell}^{\ell} c_{n\ell m}\Psi_{n\ell m}(R\mathbf{r}) \tag{8}$$

where the $c_{n\ell m}$ are the transform coefficients of E in Eq. (3), and the $\Psi_{n\ell m}$ are the functions given in Table 1.

Table 2
$\upsilon_{\ell m}$ coefficients for the ODF closed formulae (see Eq. (9)). For SPF basis: P_l is the Legendre polynomial of order l. For SoH basis: ${}_2F_1$ is the Gauss hypergeometric function. For SoH basis: $n!! = (n)(n-2)\cdots(4)(2)$, $J_n(x)$ is the Bessel function of order n, Z a normalization constant and q_{max} the maximum q-value used during the acquisition.

SPF	$\frac{1}{\sqrt{4\pi}}\delta(l)\delta(m) - \frac{1}{8\pi}\sum_{n=1}^{N}\sum_{i=1}^{n}(-1)^i\left[\frac{2n!}{\zeta^{\frac{3}{2}}\Gamma(n+\frac{3}{2})}\right]^{\frac{1}{2}}\binom{n+\frac{1}{2}}{n-i}\frac{2^i}{i!}P_\ell(0)(-\ell)(\ell+1)c_{n\ell m}$ (Cheng et al., 2010a)
SPFdual	$\sum_{n=0}^{N}2\zeta^{3/4}(-1)^n c_{nlm}\left[\frac{\Gamma(n+3/2)}{n!}\right]^{1/2}$ (Appendix B)
SoH	$(-1)^{l/2}(\frac{2^l\pi^{l-1}}{(2l-1)!!}\binom{l+1}{l+1}\frac{b_{max}^{l+1}}{l+1})c_{\ell m} - \frac{(l-1)!!}{2\pi q_{max}^{l+1}2^{l/2}(l/2-1)!}c_{\ell m} + \frac{1}{2\pi}\frac{(l+1)!!}{2^{l/2}(l/2)!}d_{\ell m})$ (Descoteaux et al., 2011)
SHORE	$\sum_{n=0}^{N}c_{n\ell m}\frac{(-1)^{n-l/2}}{2(4\pi^2\zeta)^{3/2}}\left[\frac{2(4\pi^2\zeta)^{3/2}(n-l)!}{\Gamma(n+3/2)}\right]^{1/2}\frac{\Gamma(\ell/2+3/2)\Gamma(3/2+n)}{\Gamma(l+3/2)(n-l)!}(\frac{1}{2})^{-\ell/2-3/2}{}_2F_1(-n+l,l/2+3/2;l+3/2;2)$ (Appendix C)

Moreover, defining the ODF Υ as the integration of the EAP over a solid angle as given by Eq. (2), we can also derive a closed formula for the ODF in terms of real and symmetric Spherical Harmonic (SH) basis functions:

$$\Upsilon(\mathbf{r}) = \sum_{\ell=0}^{L}\sum_{m=-\ell}^{\ell}\upsilon_{\ell m}Y_\ell^m(\mathbf{r}) \tag{9}$$

where $Y_\ell^m(\mathbf{u})$ is the SH function of order ℓ and degree m and the coefficients $\upsilon_{\ell m}$ are those given in Table 2

3. CS properties

The Compressed Sensing acquisition process has been proven useful in recovering Magnetic Resonance (MR) images by significantly undersampling their k-spaces (Lustig et al., 2007; Guo and Yin, 2010; Ganesh et al., 2008; Chartrand, 2009). (Donoho, 2006; Candes and Wakin, 2008) described a complete mathematical framework of the CS theory.

In diffusion MRI, some attempts to reconstruct EAP using CS have been proposed by Merlet and Deriche (2010), Saint-Amant and Descoteaux (2011), Menzel et al. (2011). However, these works come in a discrete framework and diffusion features have to be numerically computed. Others approaches to continuously represent, a part or the entire, diffusion process have also been done using CS (Michailovich and Rathi, 2010; Rathi et al., 2011; Tristán-Vega and Westin, 2011). In (Michailovich and Rathi, 2010; Tristán-Vega and Westin, 2011), the authors work with measurements taken at same radii and only estimate the ODF. In (Rathi et al., 2011), the authors estimate the diffusion signal via a multiple shells acquisition but does not provide any analytical formula to estimate the EAP or the ODF. Here, we consider a CS reconstruction combined with a continuous representation of the diffusion signal and available closed formulae to estimate both the EAP and the ODF. Some works (Merlet et al., 2011b; Cheng et al., 2011b) have been published towards this. (Merlet et al., 2011b) is about CS recovering in the SPFdual basis and (Cheng et al., 2011b) is about CS recovering in the SPF basis. These two papers give a first experimental insight of CS capabilities in dMRI.

Compressed Sensing (CS) asserts that one can recover certain signals from fewer measurements than traditional methods. In order to make possible the signal recovering, CS relies on several properties:

- The **incoherence**. It expresses the idea that the signal of interest must be spread out in the acquisition domain.
- The **sparsity**. It expresses the idea that the signal information is contained in a small number of coefficients.
- An ℓ_1-**minimization** recovery combined with an **efficient sampling protocol**.

In this section, we present the theoretical aspect of the CS theory (Donoho, 2006; Cands and Romberg, 2007; Candès, 2008; Candes and Wakin, 2008; Donoho, 2010; Candes and Plan, 2011) and describe, when possible, the extension to a continuous framework. We also highlight theoretical and experimental comparisons between the bases introduced in Section 2. We choose these four bases mainly because: (1) They are the most commonly used in the dMRI field; (2) They enable a continuous representation of the diffusion signal; and (3) They provide analytical formulae for estimating the EAP and the ODF. We introduce the notations in stages. Note that this work is by no means a theoretical CS framework for continuous signal. We only show that some results obtained in the classical and discrete CS theory can be extended to the reconstruction of continuous signal.

3.1. On the incoherence property of CS bases

Let us consider the $M \times n$ orthonormal basis matrix, i.e. a matrix whose columns form an orthonormal basis

$$\mathbf{A} = \begin{pmatrix} a_{11} & \cdots & a_{1n} \\ \vdots & \ddots & \vdots \\ a_{M1} & \cdots & a_{Mn} \end{pmatrix}. \tag{10}$$

We are in the general setting where we want to recover a S-sparse signal $\mathbf{x} \in \mathcal{R}^n$ from an observation vector $\mathbf{y} \in \mathcal{R}^M$, such that

$$\mathbf{y} = \mathbf{A}\mathbf{x} \tag{11}$$

Because $\mathbf{x}$ is S-sparse (only S components are non-zeros), we need that $\mathbf{A}$ admits a certain amount of incoherence to guaranty its recovery. In this section we focus our attention on this incoherence property.

For a particular application, the sensing matrix $\mathbf{A}$ can be decomposed as a product of a sparsity basis $\mathbf{\Psi}$ and an orthogonal measurement system $\mathbf{\Phi}$ (Cands and Romberg, 2007, Donoho, 2006), i.e. $\mathbf{A} = \mathbf{\Phi}\mathbf{\Psi}$. In this case, we can write μ as

$$\mu(\mathbf{\Phi}, \Psi) = max_{kj}| < \phi_k, \psi_j > |,$$

where ϕ_k and ψ_j are the columns of $\mathbf{\Phi}$ and $\mathbf{\Psi}$. This is sometime referred to as mutual coherence (Candes and Wakin, 2008). In our setting, we want to reconstruct the diffusion signal directly from its measures in the q-space. Therefore, the measurement system is the canonical or spike basis, i.e. $\mathbf{\Phi} = I$ and $\phi_k = \delta_k$. Considering this point, we define the coherence parameter as Cands and Romberg (2007), i.e.

$$\mu(\mathbf{A}) = \max_{1\leqslant i\leqslant M, 1\leqslant j\leqslant n}|a_{ij}| \tag{12}$$

$\mu(\mathbf{A}) \in \left[\frac{1}{\sqrt{M}}, 1\right]$. Lower is $\mu(\mathbf{A})$ and higher is the incoherence of $\mathbf{A}$. The upper bound is easily derived using the fact that a component value of a column vector cannot exceed the norm of this vector (equal to 1 in our case). The lower bound is the special case where all the column vector components have the same values $a_{1j} = \cdots = a_{Mj}$ for $j \in [1,n]$, that is this vector is flat. Hence, $\sqrt{\sum_{i=1}^{M}a_{ij}^2} = \sqrt{Ma_{1j}^2} = 1$, which comes to $a_{1j} = \ldots = a_{Mj} = \frac{1}{\sqrt{M}}$.

We can interpret $\mu(\mathbf{A})$ as how the energy of a basis function is concentrated. Higher $\mu(\mathbf{A})$ and more concentrated the energy of the corresponding column. A high concentration results in

constraining the significant information of the signal to recover $\mathbf{x}$ on few measurements. On the contrary, if the vector energy is little concentrated (flat function), then the information in x is spread out on the observation.

In order to better understand this coherence parameter, let us see an example. Suppose $\mathbf{x} \in \mathcal{R}^n$ is S-sparse with $S = 1$. The non-zero coefficients is the ℓ^{th} with $\ell \in [1, n]$. Then

$$\begin{pmatrix} y_1 \\ \cdot \\ \cdot \\ \cdot \\ y_M \end{pmatrix} = \begin{pmatrix} a_{11} & \cdots & a_{1n} \\ \cdot & & \cdot \\ \cdot & & \cdot \\ \cdot & & \cdot \\ a_{M1} & \cdots & a_{Mn} \end{pmatrix} \begin{pmatrix} 0 \\ \cdot \\ x_\ell \\ \cdot \\ 0 \end{pmatrix} = \begin{pmatrix} a_{1\ell}x_\ell \\ \cdot \\ \cdot \\ \cdot \\ a_{M\ell}x_\ell \end{pmatrix}. \tag{13}$$

Suppose that $a_{k\ell} = 1$ with $k \in [1, M]$. It means that $\mu(\mathbf{A})$ reaches its upper bound. Because the column of $\mathbf{A}$ has an ℓ_2 norm equal to 1, $a_{i\ell} = 0$ for any $i \neq k$. Then

$$\begin{pmatrix} y_1 \\ \cdot \\ y_k \\ \cdot \\ y_M \end{pmatrix} = \begin{pmatrix} 0 \\ \cdot \\ a_{k\ell}x_\ell \\ \cdot \\ 0 \end{pmatrix} = \begin{pmatrix} 0 \\ \cdot \\ x_\ell \\ \cdot \\ 0 \end{pmatrix}. \tag{14}$$

In this case, we are constrained to observe y_k, otherwise $\mathbf{x}$ disappears.

Now, suppose $\mu(\mathbf{A})$ reaches its lower bound. It means $\mathbf{A}$ is a flat matrix with every component equal to $\frac{1}{\sqrt{M}}$. Then

$$\begin{pmatrix} y_1 \\ \vdots \\ y_M \end{pmatrix} = \frac{1}{\sqrt{M}} \begin{pmatrix} x_\ell \\ \vdots \\ x_\ell \end{pmatrix}. \tag{15}$$

In this case, we can sample at any location and still have information about x_l. The information of $\mathbf{x}$ is spread out on the observation.

3.1.1. Why is this incoherence property crucial in Compressed Sensing recovery?

The aim of Compressed Sensing is to infer a S-sparse signal $\mathbf{x} \in \mathcal{R}^n$ from an observation vector of size $m \ll n$. On this purpose, we take m rows of an orthonormal basis matrix $\mathbf{A} \in \mathcal{R}^{M \times n}$ according to a subset $\Omega \subset \{1, \ldots, M\}$ of size $card(\Omega) = m$ (Donoho, 2010). This gives a matrix $\mathbf{A}_\Omega \in \mathcal{R}^{m \times n}$ and a vector $\mathbf{y}_\Omega \in \mathcal{R}^m$ consisting, respectively, of the rows of $\mathbf{A}$ and the element of $\mathbf{y}$ indexed by Ω. Then, we solve this highly underdetermined system

$$\mathbf{y}_\Omega = \mathbf{A}_\Omega \mathbf{x} \tag{16}$$

Due to the small number of measurements m, it is obvious that a low coherence is crucial to recover $\mathbf{x}$. We prefer the information to be spread out in the observable domain. We cannot take the risk to see $\mathbf{y}_\Omega$ disappears because the measurements are not properly localized (see case where μ reaches its upper bound above). Hence, $\mu(\mathbf{A})$ directly influences the number of acquisitions.

3.1.2. Evaluation of incoherence

Eq. (12) comes to search for the maximum of all the CS basis elements. Before going any further, we need to fix (1) the scale parameter ζ in the SPF (Eq. (4)), SPFdual (Eq. (5)) and SHORE (Eq. (6)) bases and (2) the bases orders n, ℓ. First, the zeroth order radial function of these bases should have a Gaussian shape dependent on the signal attenuation $E(q) = \exp(-4\pi^2 \tau q^2 D)$ with τ the time diffusion constant characteristic of the acquisition process and D the mean diffusivity constant. Considering the SPF and SHORE bases, we obtain the same zeroth order radial function

$$\begin{aligned} K_{000}(q\mathbf{u}) &= \left[\frac{2}{\zeta^{3/2}\Gamma(3/2)}\right]^{1/2} \exp\left(\frac{-q^2}{2\zeta}\right) L_0^{1/2}\left(\frac{q^2}{\zeta}\right) \\ &= Const. \exp\left(\frac{-q^2}{2\zeta}\right). \end{aligned} \tag{17}$$

Then, the scale parameter is given by setting $\exp\left(\frac{-q^2}{2\zeta}\right) = \exp(-4\pi^2\tau q^2 D)$, i.e. $\zeta = \frac{1}{8\pi^2\tau D}$. Now considering the SPF-dual basis, we get the zeroth order radial function

$$\begin{aligned} K_{000}(q\mathbf{u}) &= 4\frac{\zeta^{3/2}\pi^{3/2}}{\Gamma(3/2)}\left[\frac{1}{\zeta^{\frac{3}{2}}\Gamma(\frac{3}{2})}\right]^{\frac{1}{2}} \Gamma\left(\frac{3}{2}\right) {}_1F_1\left(\frac{3}{2}, \frac{3}{2}, -2(\pi q)^2\zeta\right) \\ &= Const. {}_1F_1\left(\frac{3}{2}, \frac{3}{2}, -2(\pi q)^2\zeta\right) \\ &= Const. \exp(-2(\pi q)^2\zeta). \end{aligned} \tag{18}$$

We get $\zeta = 2\tau D$. Secondly, we fix each basis order in such way they enable to model many diffusion profiles. Then, for SPF and SPF dual bases we set an angular order $\ell = 6$ and a radial order $n = 5$, which give 140 atoms for each basis respectively. For the SoH basis, we set an angular order $\ell = 6$, which gives 56 atoms (the radial order is fixed and equal to 2). For SHORE basis, the radial order is $n = 6$ and because $\ell$is bounded by n, this gives 72 atoms. On the whole, experiments show that we do not need a higher angular order to accurately model the angular diffusion profiles.

Now, we are able to measure the coherence μ (Eq. (12)) for each basis. You should note that this measure depends directly on the scale parameter ζ in Eqs. (4) and (6). ζ itself depends on the diffusion constant τ and the mean diffusivity constant D. We use common values for these parameters: $\tau = 1/4\pi^2$ and D is in range $[0.1 \times 10^{-3}, 2 \times 10^{-3}]$. Recall that μ is computed on orthonormal bases, so we need to numerically normalize the atom of the SoH basis using the ℓ_2 norm.

Fig. 1 gives the evaluation of the coherence μ while choosing the CS matrix as the SPF, SPFd, SoH and SHORE basis with the parameters described above. We see that SHORE basis (red curve) and SPFdual basis (green curve) have the lowest coherence values (then the highest incoherence). The coherence of the SPF basis (blue curve) is approximately twice the coherence of the latter bases and the coherence of the SoH basis is constant because it does not depend on D. For the following experiments (in Section 4), we fix ζ with respect to both the mean diffusivity D (which is peculiar to a given diffusion signal) and the diffusion constant τ (which is used during the acquisition) (see Fig. 2).

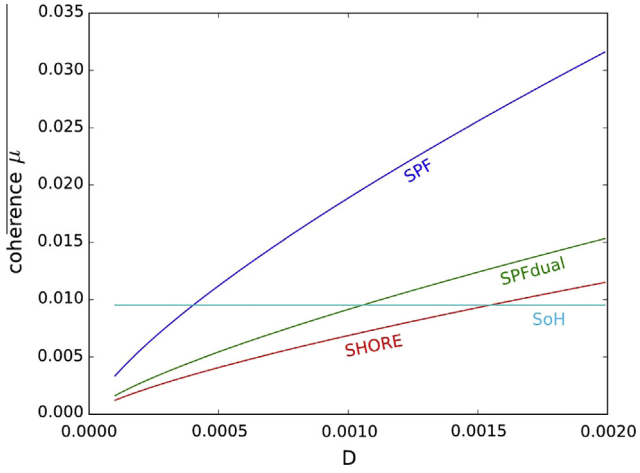

Fig. 1. Coherence μ of the SPF, SPF dual, SoH and SHORE basis.

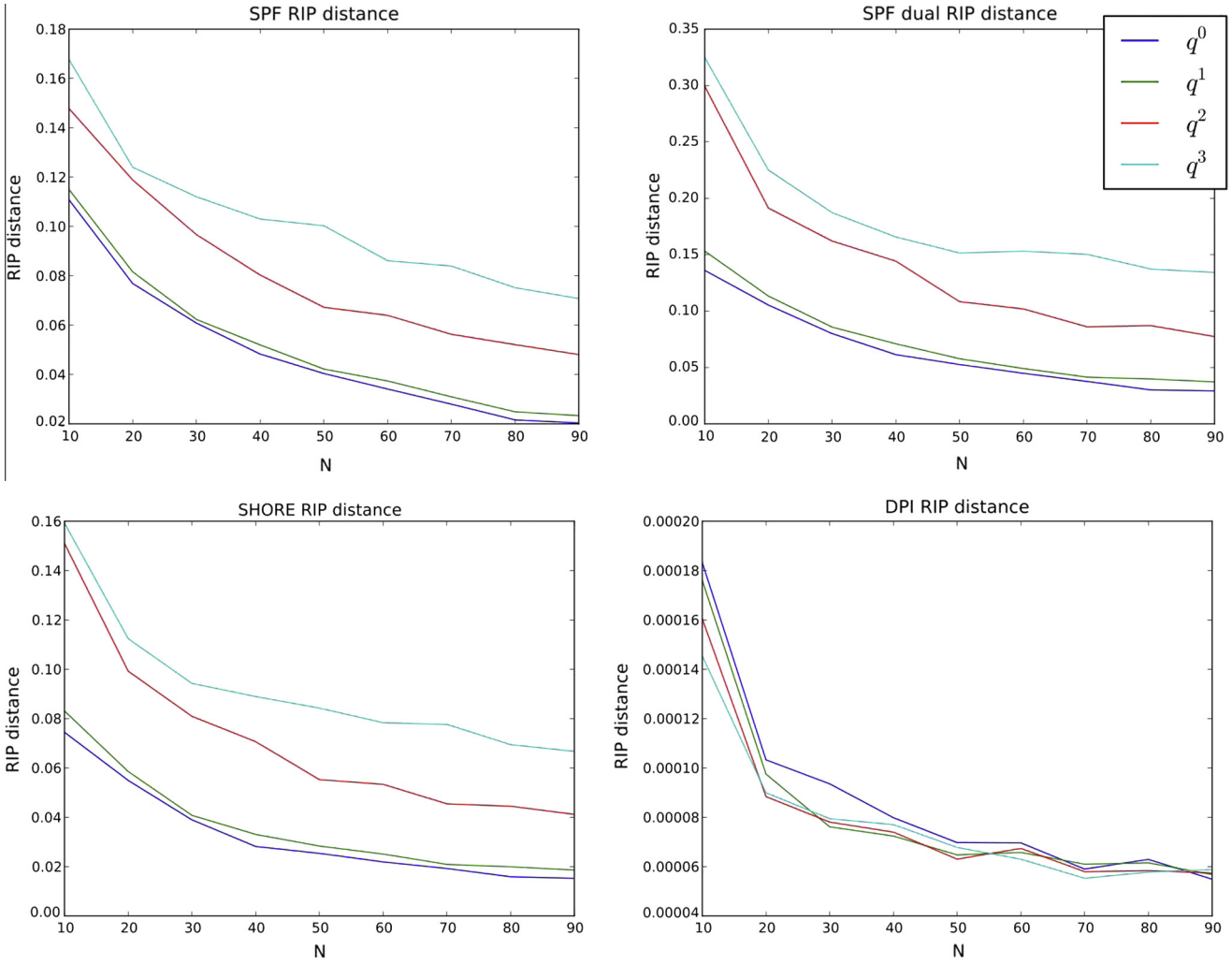

Fig. 2. pRIP distance evaluated for the SPF, SPFdual, SoH and SHORE bases. We considered four sampling schemes following radial distributions in q^γ with $\gamma = 1, 2, 3, 4$ and compute δ while taking $N = 10$–90 measurements.

3.2. On the sparsity of CS bases

A basis, which gives sparse representations of signals in a given domain, is considered as a basis that correctly fit the corresponding signals. Sparse representation provide high performance for application in compression. For instance, the discrete cosine transform as well as the wavelet transform are both sparse transforms respectively used in JPEG and JPEG2000 image compression standards.

In this section, we first define what is sparsity and then evaluate the sparsity of the CS bases introduced in Section 2.

3.2.1. What is sparsity?

The sparsity expresses the idea that a signal has a compact representation, that is this signal contains a small number of non-zero coefficients. Pure sparse signals are not always available, so we redefine this notion of sparsity: We say a signal is sparse when the most significant signal information is concentrated on few coefficients, the others being relatively small.

3.2.2. Evaluation of the sparsity

In practice, we have an observation vector $\mathbf{y} \in \mathbb{R}^M$ (In our case the diffusion signal) and we look for its sparse representation $\mathbf{x} \in \mathbb{R}^n$, in a given basis represented by an orthonormal basis matrix $\mathbf{A} \in \mathcal{R}^{M \times n}$, such that $\mathbf{y} = \mathbf{A}\mathbf{x}$ (see Eq. (11)). Then, we define the sparsity of $\mathbf{x}$ as the number of basis atoms, associated with the largest coefficient of $\mathbf{x}$, which enables to correctly estimate the observation signal $\mathbf{y}$. By correct representation, we mean the normalized mean square error (NMSE) between the original observation signal $\mathbf{y}$ and the estimated observation signal $\tilde{\mathbf{y}}$ is less or equal to 1×10^{-2}.

$$NMSE = \frac{\|\mathbf{y} - \tilde{\mathbf{y}}\|_{\ell 2}^2}{\|\mathbf{y}\|_{\ell 2}^2} \tag{19}$$

Then, we progressively estimate $\tilde{\mathbf{y}}$ with the atoms of the given basis associated with the most important coefficients until we reach a NMSE of $1e^{-2}$. On this purpose, we need to get the coefficients vector $\mathbf{x}$ such that $\mathbf{y} = \mathbf{A}\mathbf{x}$. The question in this section is not which basis or which reconstruction method gives the best evaluation of the diffusion signal. We only want to fairly compare the sparse properties of the four bases (SPF, SPFdual, SoH and SHORE). To do that, we evaluate $\mathbf{x}$ in the least square sense by considering an overdetermined system, i.e. the number of measurements $M \gg n$. In this case, and only because the system is overdetermined, we do not need any regularization (l_1 or l_2 regularization) for the evaluation of $\mathbf{x}$. It comes to compute $\mathbf{x} = (\mathbf{A}^T\mathbf{A})^{-1}$-

$\mathbf{A}^T\mathbf{y}$, where $\mathbf{A} \in \mathbb{R}^{n\times M}$ represent one of the four bases. We set $M = 10{,}000$ measurements uniformly spread between $b_{min} = 0$ and $b_{max} = 10{,}000$ s mm^{-2} (beyond this value the signal is considered to be equal to zero).

Table 3 gives the averaged number of atoms necessary to correctly estimate Gaussian-based diffusion signals (see Appendix A) in the SPF, SPFdual, SoH and SHORE bases with the order previously defined in Section 3.1. The number of atoms is averaged for several diffusion profiles (one fiber, 90°-crossing fibers case and 60°-crossing fibers). We have repeated the experiments, while increasing the radial and angular order and similar results were obtained.

For SPF basis, approximately 12.67 atoms are necessary to correctly reconstruct a diffusion signal with a NMSE less or equal to $1e^{-2}$. SPFdual basis is not as sparse as SPF basis. However, it does not mean that the quality of the diffusion signal modeled in the SPFdual basis will be worse than the one modeled in SPF basis. The quality of the estimation depends on other parameters (Recovery method, coherence of the basis). SoH is not sparse according to our criteria. SHORE basis obviously gives the best sparse property in modeling diffusion signal. Nearly half the number of coefficients are necessary compared to SPF basis. We have repeated the experiments, with a NMSE less or equal to $1e^{-2}$, which lead to the same conclusion.

3.3. CS recovery

Let us remind the context. We want to recover a S-sparse signal $\mathbf{x} \in \mathcal{R}^n$ from an observation vector $\mathbf{y}_{\mathbf{\Omega}} \in \mathcal{R}^m$ with $m < n$, such that

$$\mathbf{y}_{\mathbf{\Omega}} = \mathbf{A}_{\mathbf{\Omega}}\mathbf{x} \tag{20}$$

$\mathbf{A}_{\mathbf{\Omega}} \in \mathcal{R}^{m\times n}$ is called the CS matrix. $\mathbf{\Omega}$ defines a subset of indices corresponding to samples in which $\mathbf{A}_{\mathbf{\Omega}}$ is evaluated and $\mathbf{y}_{\mathbf{\Omega}}$ is acquired. This problem is ill-posed because we have fewer equations than unknowns ($m < n$). However, if $\mathbf{x}$ is sufficiently sparse, one can recover $\mathbf{x}$ in Eq. (20) by solving the following convex optimization problem (Donoho, 2006; Candes and Wakin, 2008):

$$\min_{\mathbf{x}\in\mathcal{R}^n} \|\mathbf{x}\|_{\ell_1} \quad \text{subject to} \quad \mathbf{y}_{\mathbf{\Omega}} = \mathbf{A}_{\mathbf{\Omega}}\mathbf{x} \tag{21}$$

where $\mathbf{y}_{\mathbf{\Omega}} = \mathbf{A}_{\mathbf{\Omega}}\mathbf{x}$ is the data consistency constraint, $\|\mathbf{x}\|_1$ is the sparsity constraint. The data consistency constraint enables the solution to remain close to the raw data acquisition, whereas the minimization of the second term promotes sparsity. In short, this mathematical problem searches for the sparsest solution while remaining close to the acquired data.

In this section, we first present some theoretical results on the accuracy of the reconstruction (Candes and Wakin, 2008), which mainly rely on the Restricted Isometry Property (RIP). Finally, we propose a method to evaluate the sampling scheme via a partial computation of the RIP.

3.3.1. How accurate is the reconstruction?

Reference (Candès, 2008) established some results about the accuracy of the CS reconstruction of a sparse signal $\mathbf{x}$ at the condition that the sensing matrix $\mathbf{A}_{\mathbf{\Omega}}$ obeys the RIP, with an isometry constant defined as:

Table 3
Number of atoms necessary to correctly estimate Gaussian-based diffusion signal in the SPF, SPFdual, SoH and SHORE bases. These results are averaged for several diffusion profiles (one fiber, 90°-crossing fibers case and 60°-crossing fibers).

	SPF	SPFdual	SoH	SHORE
Number of atoms	12.67	17	34.67	7.33

Definition 1. For each integer $s = 1, 2, \ldots$, we define the isometry constant δ_s of a matrix $\mathbf{A}_{\mathbf{\Omega}}$ as the smallest number such that

$$(1-\delta_s)\|\mathbf{x}\|_{\ell_2} \leqslant \|\mathbf{A}_{\mathbf{\Omega}}\mathbf{x}\|_{\ell_2} \leqslant (1+\delta_s)\|\mathbf{x}\|_{\ell_2} \tag{22}$$

holds for all S-sparse vectors, that is vectors that have at most s non-zero entries.

In particular, (Candès, 2008) proved, for $\delta_{2s} < \sqrt{2}-1$ and noiseless recovery, that the solution x^* of Eq. (21) obeys:

$$\|\mathbf{x}^* - \mathbf{x}\|_{\ell_2} \leqslant C_0 s^{-1/2}\|\mathbf{x}_s - \mathbf{x}\|_{\ell_1}, \tag{23}$$

with C_0 a constant and x_s the best sparse approximation knowing exactly the locations and amplitudes of the s-largest entries of $\mathbf{x}$. Then, if $\mathbf{x}$ has exactly s non-zero coefficients, the solution is exact. This bound is given for noiseless recovery.

When x is corrupted by noise $\mathbf{z} \in \mathcal{R}^m$, that is

$$\mathbf{y} = \mathbf{A}_{\mathbf{\Omega}}\mathbf{x} + \mathbf{z}, \tag{24}$$

we relax the constraint in Eq. (21) and solve

$$\min_{\mathbf{x}\in\mathcal{R}^n} \|\mathbf{x}\|_{\ell_1} \quad \text{subject to} \quad \|\mathbf{y} - \mathbf{A}_{\mathbf{\Omega}}\mathbf{x}\|_{\ell_2} \leqslant \epsilon \tag{25}$$

where ϵ is the level of noise in the data. For given noisy data, the error between $\mathbf{x}^*$ and $\mathbf{x}$ is

$$\|\mathbf{x}^* - \mathbf{x}\|_{\ell_2} \leqslant C_0 s^{-1/2}\|\mathbf{x}_s - \mathbf{x}\|_{\ell_1} + C_1\epsilon \tag{26}$$

with C_0 and C_1 two constants and ϵ the noise level such that $\|\mathbf{z}\|_2 \leqslant \epsilon$. (Candès, 2008) still assumes that result in Eq. (26) holds for $\delta_{2s} < \sqrt{2}-1$.

Note that a recent work (Cands et al., 2011) was published to generalize the CS theory described in (Candes and Wakin, 2008). (Cands et al., 2011) shows that it is also possible to recover signals (within the bound given in Eq. (26)) which are sparse in an overcomplete dictionary, when the sensing matrix $\mathbf{A}$ satisfies the D-RIP (a generalization of the RIP) with an isometry constant $\delta_{2s} < 0.08$. However, in our work, we consider the diffusion signal sparse with respect to an orthonormal basis, and Candes and Wakin (2008) provides the same bound on the accuracy of the reconstruction with an isometry constant $\delta_{2s} < \sqrt{2}-1$, which is less constrained and more easily satisfied than $\delta_{2s} < 0.08$. Then, the technique described in Candes and Wakin (2008) is more appropriate for our case.

3.3.2. How to choose the measurements?

The RIP sets a condition in order to well define the sensing matrix $\mathbf{A}_{\mathbf{\Omega}}$. In other words, it allows us a us to evaluate the efficiency of our sampling scheme to obtain accurate reconstruction (together with the condition that the signal of interest is sparse). The RIP leads to the fact that all subsets of s columns taken from $\mathbf{A}_{\mathbf{\Omega}}$ are nearly orthogonals. Hence, a way to evaluate whether or not the RIP holds, is to search for group of nearly orthogonal columns. This intensive procedure is performed by taking the dot product between every column of the matrix $\mathbf{A}_{\mathbf{\Omega}}$ and, then, counting the size of each group of orthogonal vector. Larger is this size more the RIP holds. In order to clarify this point, we present an example for reconstructing a S-sparse signal with $S = 2$, where the non-zero entries are the lth and kth. We have

$$\mathbf{Ax} = \begin{pmatrix} a_0(0) & \cdots & a_n(0) \\ \cdot & & \cdot \\ \cdot & & \cdot \\ \cdot & & \cdot \\ a_0(m) & \cdots & a_n(m) \end{pmatrix} \begin{pmatrix} 0 \\ x_l \\ 0 \\ x_k \\ 0 \end{pmatrix} = \begin{pmatrix} a_l(0)x_l + a_k(0)x_k \\ \cdot \\ \cdot \\ \cdot \\ a_l(m)x_l + a_k(m)x_k \end{pmatrix}. \tag{27}$$

If a_l and a_k are orthogonals, i.e. $\langle \mathbf{a}_l \cdot \mathbf{a}_k \rangle = 0$, then $\mathbf{a}_l$ and $\mathbf{a}_k$ are linearly independent, i.e. $\lambda_l \mathbf{a}_l + \lambda_k \mathbf{a}_k \neq 0, \quad \forall (\lambda_l, \lambda_k) \in \mathcal{R}^2$. If $\langle \mathbf{a}_l \cdot \mathbf{a}_k \rangle \neq 0$, then it may be a sparse vector $\mathbf{x}$ such that $x_l \mathbf{a}_l + x_k \mathbf{a}_k = 0$, i.e. x lies in the nullspace of $\mathbf{A}_{\boldsymbol{\Omega}}$. To avoid this, we want that every subset of columns of $\mathbf{A}_{\boldsymbol{\Omega}}$ to be orthogonal. By generalizing this example, it is easy to understand that larger are the groups of orthogonal columns in $\mathbf{A}_{\boldsymbol{\Omega}}$, lower the risk that $\mathbf{x}$ lies in the nullspace of the sensing matrix $\mathbf{A}_{\boldsymbol{\Omega}}$ Hence, the RIP property ensures that $\mathbf{x}$ lies away from the nullspace of the sensing matrix.

Unfortunately, the columns of the sensing matrix are never truly orthogonal and it would be very time consuming to evaluate the orthogonality of every subset of columns taken from $\mathbf{A}_{\boldsymbol{\Omega}}$. Instead of doing that, we propose to compute what we call a partial RIP (pRIP) distance. For this purpose, we randomly choose columns from $\mathbf{A}_{\boldsymbol{\Omega}}$. Let call $\mathcal{A}_{\tau_r} = \{a_{rand(2,n)}\}$ (n is the number of columns of $\mathbf{A}_{\boldsymbol{\Omega}}$) one subset of columns randomly taken from $\mathbf{A}_{\boldsymbol{\Omega}}$. The number of column vectors in $\mathcal{A}_{\tau_r}$, i.e. card $(\tau_r) = T$, is also set as random such that $1 < T \leqslant n$. Then, we define the quantity $\delta_{\tau_r} = \frac{1}{T} \sum_{\substack{i,j \subset \tau_r \\ i \neq j}} \langle a_i, a_j \rangle$, which represents the mean of the dot product between every vector in $\mathcal{A}_{\tau_r}$. The pRIP distance is given as $pRIP(\mathbf{A}_{\boldsymbol{\Omega}}) = \frac{1}{R} \sum_{r=0}^{R} \delta_{\tau_r}$ with R the number of subset to evaluate. It is easy to see that the pRIP can take its value between 0 (when all the columns of $\mathbf{A}_{\boldsymbol{\Omega}}$ are pairwise orthogonal) and 1 (when all the columns of $\mathbf{A}_{\boldsymbol{\Omega}}$ are identical). In practice and for our experiments, we have found that the pRIP distance is well computed for $R = 1000$.

Formally, we can state the problem as follow: We look for the subset of samples Ω such that

$$\Omega = \arg\min_{\Omega} pRIP(\mathbf{A}_{\boldsymbol{\Omega}}) \tag{28}$$

We use this property to evaluate the efficiency and the robustness of our sampling scheme and the underlying sensing matrix.

4. Experimental results

The first part of the experiments concerns the reconstruction of synthetic data. Synthetic data allows us to evaluate (1) a sampling protocol (Section 4.1) and (2) the robustness to noise (Section 4.2). More particularly in Section 4.2, we present experiments on diffusion signal and ODF reconstruction (Section 4.2.2 and Section 4.2.1), and compare the EAP based CS recovery with the EAP computed via the DSI technique (Section 4.2.3). Then, we show results on a monkey brain (Section 4.3) data and phantom data (Section 4.4). In all the experiments, we set the scale parameter ζ and the bases order as in Section 3.1, i.e. an angular order $\ell = 6$ and a radial order $n = 5$ for SPF and SPF dual bases, a radial order of $n = 6$ for SHORE basis and an angular order of $\ell = 6$ for SoH basis. ζ changes along with the mean diffusivity constant D, peculiar to a given diffusion signal. For the synthetic experiments we set $D = 0.7e{-}3$ and ζ is respectively set to 700, $3.5462e{-}5$, 700 for SPF, SPFdual and SHORE bases (For details on these values, see Section 3.1). For the experiments on the monkey and phantom data, we will fix ζ with the mean diffusivity constant averaged on voxels in the region of interest.

Before going any further, we give the notations and materials used in the experimental part. We also describe the ℓ_1 minimization problem (called ℓ_1 recovery in the following), which is used in CS recovery. Then, we describe the least square recovery with an ℓ_2 regularization (called ℓ_2 recovery in the following), which is used for comparison.

Notations

We represent the normalized diffusion signal $E(q\mathbf{u})$ as a truncated linear combination of $\Phi_{n\ell m}(q\mathbf{u})$ with n the radial order, $\ell$and m the angular order and degree, i.e.

$$E(q\mathbf{u}) = \sum_{n=0}^{N} \sum_{\ell=0}^{L} \sum_{m=-\ell}^{\ell} c_{n\ell m} \Phi_{n\ell m}(q\mathbf{u}), \tag{29}$$

where the $c_{n\ell m} = \langle E, \Phi_{n\ell m} \rangle$ are the transform coefficients. We call n_c the total number of atoms.

Suppose n_q is the number of measurements, $\mathbf{E} \in \mathcal{R}^{n_q}$ a vector representing the diffusion signal, $\mathbf{c} \in \mathcal{R}^{n_c}$ the vector of transform coefficients $c_{n\ell m}$ and $\boldsymbol{\Phi} \in \mathcal{R}^{n_q \times n_c}$ the matrix constructed with the atoms of the given basis as

$$\boldsymbol{\Phi} = \begin{pmatrix} \Phi_{000}(q_1 \mathbf{u_1}) & \cdots & \Phi_{NLL}(q_1 \mathbf{u_1}) \\ \vdots & \ddots & \vdots \\ \Phi_{000}(q_{n_q} \mathbf{u_{n_q}}) & \cdots & \Phi_{NLL}(q_{n_q} \mathbf{u_{n_q}}) \end{pmatrix}. \tag{30}$$

We can write equation Eq. (29) as a linear system of overdetermined equations

$$\mathbf{E} = \boldsymbol{\Phi} \mathbf{c}. \tag{31}$$

The aim is to recover $\mathbf{c}$ given the normalized diffusion signal $\mathbf{E}$ and the matrix $\boldsymbol{\Phi}$. Then, the EAP and ODF can be analytically computed from $\mathbf{c}$ using the closed forms given in Section 2.

ℓ_1 recovery

In order to find $\mathbf{c}$, we solve the convex optimization problem, specified in Eq. (21), i.e.

$$\min_{\mathbf{c} \in \mathcal{R}^{n_c}} \|\mathbf{c}\|_{\ell_1} \quad \text{subject to} \quad \|\mathbf{E} - \boldsymbol{\Phi}\mathbf{c}\|_{\ell_2} \leqslant \epsilon. \tag{32}$$

For convenience, we replace the constraint with a penalty. It comes to solve

$$\arg\min_{\mathbf{c} \in \mathcal{R}^{n_c}} \|\mathbf{E} - \boldsymbol{\Phi}\mathbf{c}\|_{\ell_2} + \lambda \|\mathbf{c}\|_{\ell_1}, \tag{33}$$

where the regularization parameter λ replaces the noise level ϵ in Eq. (32), in governing the trade-off between the data consistency and its sparsity. We solve the problem by means of a Fast Iterative Shrinkage-Thresholding Algorithm (FISTA) (Beck and Teboulle, 2009; Zibulevsky and Elad, 2010), an iterative algorithm where each iteration involves a shrinkage step. We chose this algorithm because of its efficiency, its speed and its convergence.

Appropriate choice of the regularization parameter λ is a critical issue in ℓ_1 recovery. The regularization parameter selection in Eq. (33) depends essentially on the level of noise, the data sparsity and the number of measurements. Then, we need a technique that adaptively chooses λ, i.e. for each instance of diffusion signal contained in a whole data set. We use cross validation to assess the reconstruction parameters (Ward, 2009). In particular, we use a K-fold Cross Validation, which consists in splitting the entire data set in K subsets. $K-1$ subsets are used to reconstruct the signal, whereas the K^{th} left apart subset enables an estimation of the regularization parameter λ_K via the evaluation of a cross validation distance. This operation is repeated K times by considering the other subsets. Then, we keep an average value, $\lambda = \frac{1}{K} \sum_{k=1}^{K} \lambda_k$. This procedure is computationally extensive but experiments show that it enables a close approximation of the optimal regularization parameter. To avoid a drastic increase of the computational effort, we split our data set in five partitions, i.e. $K = 5$. Our experiments showed that it is sufficient to well evaluate λ in Eq. (33). See (Ward, 2009) for details regarding the use of cross validation in CS.

ℓ_2 recovery

Least square recovery with an ℓ_2 regularization is the common method used so far in order to solve system of overdetermined equations involving the bases in Section 2. The ℓ_2 recovery problem to solve is

$$\arg\min_{\mathbf{c}\in\mathcal{R}^{n_c}} \|\mathbf{E}-\mathbf{\Phi c}\|_{\ell_2} + \lambda_l \|\mathbf{L}\|_{\ell_2} + \lambda_n \|\mathbf{N}\|_{\ell_2}, \tag{34}$$

where $\mathbf{N} \in \mathcal{R}^{n_q \times n_c}$ and $\mathbf{L} \in \mathcal{R}^{n_q \times n_c}$ are two diagonal matrices such that $diag(\mathbf{N}) = n(n+1)$ and $diag(\mathbf{L}) = l(l+1)$. $\mathbf{L}$ is called the Laplace–Beltrami operator. These two matrices penalize the high frequencies of the radial and angular part, respectively. λ_n and λ_l enable to weight the high frequency penalization. The least square solution has a closed form given by (Assemlal et al., 2009; Ozarslan et al., 2009),

$$\mathbf{c} = (\mathbf{\Phi}^T\mathbf{\Phi} + \lambda_l \mathbf{L}^T\mathbf{L} + \lambda_n \mathbf{N}^T\mathbf{N})^{-1}\mathbf{\Phi}\mathbf{E}. \tag{35}$$

For the SoH basis (Descoteaux et al., 2011), there is only an angular regularization. Then, the least square solution is given by

$$\mathbf{c} = (\mathbf{\Phi}^T\mathbf{\Phi} + \lambda_l \mathbf{L}^T\mathbf{L})^{-1}\mathbf{\Phi}\mathbf{E}. \tag{36}$$

To enable a fair comparison with the ℓ_1 recovery, we apply a variant of cross validation, the Generalized Cross Validation (GCV) algorithm (Craven and Wahba, 1985), to assess the regularization parameters λ_l and λ_n. The GCV method is based on a K-fold cross validation, where K is the number of measurements. Fortunately, we have a closed form expression, which enables to quickly estimate λ_l and λ_n. We simply take λ_l and λ_n as the minimum argument of the GCV function, expressed as

$$\mathrm{GCV}(\lambda;\mathbf{E}) = \frac{\|\mathbf{E}-\hat{\mathbf{E}}_\lambda\|^2}{K - \mathrm{Tr}(\mathbf{S}_\lambda)}, \tag{37}$$

which makes this method very efficient. The matrix $\mathbf{S}_\lambda = \mathbf{\Phi}(\mathbf{\Phi}^T\mathbf{\Phi} + \lambda\mathbf{\Lambda})^{-1}\mathbf{\Phi}^T$ is the smoother matrix, and $\hat{\mathbf{E}}_\lambda = \mathbf{S}_\lambda\mathbf{E}$. Λ is either $\mathbf{L}^T\mathbf{L}$ or $\mathbf{N}^T\mathbf{N}$ depending on which regularization parameter we want to assess (λ_l or λ_n). With the GCV method, it is possible to adapt the regularization parameters to the data.

4.1. Sampling protocol

The quality of reconstruction is sensitive to the acquisition scheme (Merlet et al., 2011a; Caruyer et al., 2011a). In particular, the random sampling protocol usually used in CS recovery can miss information and does not ensure good reconstruction in every case. Hence, in order to remove the variance of the results due to the random aspect of the sampling scheme, it is necessary to find a robust and efficient way to acquire DW-MRIs. For this purpose, we evaluate and compare several sampling protocols. We begin by presenting some methods to distribute points on one or several spheres. It follows a presentation of the sampling schemes to be evaluated. Then, we give a first appreciation of the quality of each sampling scheme using the partial RIP (pRIP) distance presented in Section 3.3. The pRIP distance evaluates the capabilities of the sensing matrix $\mathbf{\Phi}$ to give a robust and accurate reconstruction but does not consider the signal itself. Hence, we also evaluate experimentally each sampling scheme on the reconstruction of synthetic diffusion data.

4.1.1. Jones algorithm

References (Jones et al., 1999; Deriche et al., 2009) give an algorithm to uniformly distribute N points $q_n \in R^3$ on a sphere by considering each point as an antipodal pair of electrical charges. The method involves the minimization of the electrostatic force of repulsion between each couple of charges. The electrostatic repulsion between two points q_i and q_j is given by

$$E(q_i,q_j) = \frac{1}{\|q_i+q_j\|} + \frac{1}{\|q_i-q_j\|}. \tag{38}$$

For a set of N points, the energy to minimize becomes

$$J_J = \sum_{i\neq j} E(q_i,q_j). \tag{39}$$

Reference (Cook et al., 2006) provides Camino, an Open-Source Diffusion-MRI Reconstruction and Processing software. They include several sets of directions, from $N = 3$ to 150 points, computed by electrostatic energy minimization.

4.1.2. Generalized Jones algorithm

This method is proposed by (Caruyer et al., 2011b) as a generalization of (Jones et al., 1999) to multiple shells (MS) acquisition. It enables the distribution of N points $q_n \in R^3$ on K shells of radius r_k. The points from each shell have staggered directions and follow a near-optimal uniform distribution. Another important point in this method is the possibility to balance the proportion α_k of samples between shells. We will take advantage of this feature in order to test out different radial distributions.

Firstly, the method consists in minimizing the electrostatic repulsion between every point for each shell independently, that is

$$E_1 = \sum_k r_k\alpha_k \sum_{i\neq j \ s.t \ \|q_i\|=\|q_j\|=r_k} E(q_i,q_j). \tag{40}$$

Then, in order to have staggered directions between shells, (Caruyer et al., 2011b) introduces a new term that minimizes the electrostatic repulsion of the N points projected on the unit sphere. It comes to minimize

$$E_2 = \sum_{i\neq j} \frac{1}{\left\|\frac{q_i}{\|q_i\|} - \frac{q_j}{\|q_j\|}\right\|} + \frac{1}{\left\|\frac{q_i}{\|q_i\|} + \frac{q_j}{\|q_j\|}\right\|}. \tag{41}$$

Finally, the energy to minimize is $J_{GJ} = (1-\mu)E_1 + \mu E_2$, where μ is a weighting factor.

4.1.3. Four sampling schemes

We perform our experiments on four MS sampling schemes. (Merlet et al., 2011a; Caruyer et al., 2011a) showed the advantage of taking staggered directions between shells in order to well approximate the angular profile of the diffusion process. Hence, each sampling scheme will be computed via the Generalized Jones algorithm in order to obtain staggered directions between shells. Here we, evaluate the impact of the radial distribution of the samples. Then, we test four sampling schemes where the number of samples on each shell is proportional to q^γ with $\gamma = 1, 2, 3, 4$.

4.1.4. Results on sampling protocol

We give a first appreciation of the quality of each sampling scheme using the partial RIP (pRIP) distance as described in Section 3.3. The pRIP distance roughly evaluates the efficiency of a sampling scheme to obtain accurate reconstruction. We compute it with $N = 10$ to 90 for each basis previously presented and for a sampling schemes following radial distributions in q^γ with $\gamma = 1, 2, 3, 4$. Overall, and for the SPF, SPFdual and SHORE bases, we see that the pRIP distance is higher for the schemes whose the radial distribution follow a law in q^2 and q^3 than those in q^0 and q^1. It means the schemes in q^2 and q^3 are more sensitive to noise and lead to less accurate reconstruction. The schemes in q^0 and q^1 have similar pRIP values for every number of samples N. Considering the SoH basis, the isotropy distance does not vary a lot between sampling schemes. It is also quite stable along N. It means all the sampling schemes have similar effect on the accuracy of the reconstruction while using the SoH basis.

Now, we experimentally review the outcome of multiple shells (MS) sampling on the reconstruction of synthetic data. The performance of each sampling scheme is determined on diffusion signal reconstruction while the signal is generated from a multi-tensor model (see Appendix A) through three scenarios: One fiber, two 60°-crossing fibers, two 90°-crossing fibers evaluated at b values, $b = [1000, 2000, 3000]$ s mm^{-2}. We evaluate the reconstruction for a number of samples $N = 5$–90. The quality of the diffusion signal

estimation $\widetilde{E}$ is given by the normalized mean square error (NMSE) (see Eq. (19)), evaluated on sample at b-value between 0 and 10,000, i.e. different from the measurements used for the reconstruction. We average the NMSE obtained on 1000 independent trials and for each scenario. Because this section aims to evaluate sampling schemes, and not the robustness to noise, we generate a noise-free diffusion signal. The robustness to noise was already evaluated via the computation of the isotropy distance. The results are given in Fig. 3. In this figure, we compare the ℓ_1 and ℓ_2 reconstruction methods. The curves corresponding to ℓ_1 recovery are in plain lines and the curves corresponding to ℓ_2 recovery are in dash lines. We first consider the SHORE, SPF and SPFdual bases. NMSE values for the schemes following a radial distribution in q^2 and q^3 are in line with our previous results on the pRIP distance, i.e. we get a higher NMSE for these schemes than the schemes in q^0 and q^1. Within the schemes in q^0 and q^1, we see that the NMSE for the one in q^1 remains lower than the NMSE for the one in q^0 while decreasing the number of samples N. These observations remain valid for ℓ_1 and ℓ_2 recovery. Besides, (Caruyer et al., 2011a) comes to the same conclusions regarding ℓ_2 recovery. Considering the SoH basis we have two remarks. First, the NMSE is quite the same for each radial distribution either for ℓ_2 recovery or ℓ_1 recovery. Next we observe, that ℓ_2 recovery gives lower NMSE values than ℓ_1 recovery using the SoH basis.

To resume this section, we have seen that a sampling scheme stands out for both ℓ_1 recovery and ℓ_2 recovery. This scheme uses the generalized Jones algorithm presented in Section 4.1.2, where the samples follow a radial distribution in q^1. The pRIP distance evaluated for this scheme indicates that it is robust to noise and the experiments on synthetic data show that it gives the lowest NMSE. Hence, we keep this scheme for the rest of the experiments.

4.2. Synthetic and noisy reconstruction

This section presents experiments on the reconstruction of synthetic data. We describe results from signal, ODF and EAP reconstructions, followed by a conclusion where we highlight the important points of these experiments.

4.2.1. Diffusion signal recovery

We first present results on diffusion signal recovery. Based on the previous results in Section 4.1.4, we choose a sampling scheme with a radial distribution following a law in q^1. Here, we perform experiments on diffusion signal recovery where the data is contaminated with Rician noise. As previously, we compare the ℓ_1 recovery and ℓ_2 recovery. We keep the NMSE criteria to evaluate the reconstruction of diffusion signal from a multi-tensor model Appendix A) through three scenarios: One fiber, two 60°-crossing

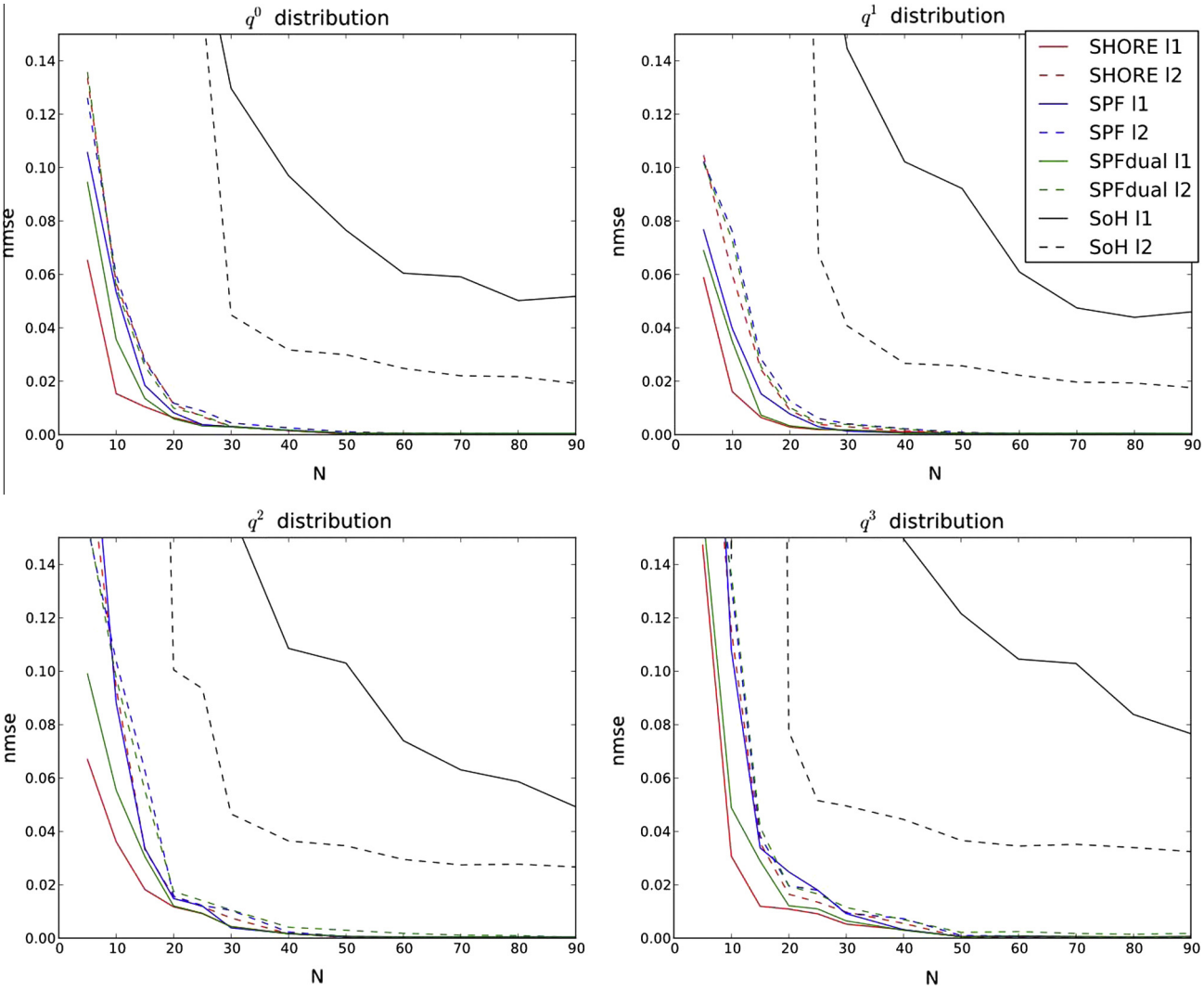

Fig. 3. NMSE evaluated for the reconstruction of synthetic data using ℓ_1 recovery (plain lines) ℓ_2 recovery (dash lines) for the SPF, SPFdual, SoH and SHORE bases. We considered four sampling schemes following radial distributions in q^γ with $\gamma = 1, 2, 3, 4$ and compute δ while taking $N = 5$–90 measurements.

fibers, two 90°-crossing fibers at b values $b = [1000, 2000, 3000]$ s mm^{-2}. We evaluate the reconstruction for a number of samples $N = 5$– 90. We add Rician noise with SNR between 30 for data contaminated with low noise level and 10 for very noisy data. The Rician noise is added to the normalized diffusion signal E in the following way: $E_{noisy} = \sqrt{(E+\epsilon_1)^2 + \epsilon_2^2}$ where $\epsilon_1, \epsilon_2 \sim \mathcal{N}(0, \sigma)$ with $\sigma = \frac{1}{SNR}$. Again, all the results are obtained on 1000 independent trials. Then, we average the results of one fiber, two 60°-crossing fibers, two 90°-crossing fibers. The resulting NMSE for ℓ_1 recovery (plain line) and ℓ_2 recovery (dash line) are presented in Fig. 4.

As expected from the preliminary results in Section 3, SPF, SPFdual and SHORE based reconstruction broadly give better results for ℓ_1 recovery than ℓ_2 recovery, and inversely for the SoH basis. This is not surprising while looking at the sparsity level of SoH basis (see Table 3 in Section 3.2). It gives the worst sparsity level with respect to the others bases. More precisely, for ℓ_2 recovery, we see a global increase of the NMSE below $N \approx 40/50$ samples at any SNR, whereas the NMSE for ℓ_1 recovery globally increases below $N = 30$ samples. For $N = 50$ and higher, the two methods lead to similar NMSE values. These results show that SHORE, SPF and SPFdual bases are appropriate for CS recovery, and enable to reconstruct diffusion signals as accurately as with ℓ_2 recovery with a smaller number of measurements. The SoH basis, however, does not enter in the CS framework and the results show that it is preferable to use the ℓ_2 recovery instead of the ℓ_1 recovery with the SoH basis.

Regarding the ℓ_1 recovery, we give a comparison on the number of samples required to correctly approximate the diffusion signal while considering the SPF, SPFdual and SHORE bases. For the same NMSE, we see that SHORE based ℓ_1 recovery needs less samples than SPF and SPFdual based ℓ_1 recovery, and that SPFdual based ℓ_1 recovery needs less samples than SPF based ℓ_1 recovery at same NMSE (see Fig. 4). For instance, to obtain a NMSE equal to 0.03 at $SNR = 30$, we need nearly 10, 16 and 18 measurements respectively for SHORE, SPFdual and SPF based reconstructions. To resume, SHORE based ℓ_1 recovery gives the best signal estimation in terms of NMSE. This results was expected from the studies regarding the coherence and sparsity of these bases in Sections 3.2 and 3.1. To quantify this result, we give the number of measurements required before a too large increase of the NMSE. We notice that approximately 20/30 measurements are needed (depending on the underlying SNR) for a SHORE based ℓ_1 recovery. This leads to approximately three times less number of measurements than in (Merlet et al., 2011b; Cheng et al., 2011b; Rathi et al., 2011).

4.2.2. Orientation Distribution Function recovery

In this section, we describe results on the angular information provided by the Orientation Distribution Function (ODF) estimated from the SPF, SPFdual and SHORE bases via the closed form presented in Section 2.2. We set apart the SoH basis due to the bad results concerning this basis in the previous section. We set up the experiments as in the previous section on diffusion signal recovery, excepted for the number of samples used for the evaluation. Here, we consider $N = 10$–90. We evaluate the angular information via two metrics: the angular error (AE) between the directions of the extracted ODF maxima and the ground truth directions, and the corresponding difference on the number of compartments (DNC) i.e. the difference between the number of maxima detected and the true number of maxima. These two metrics are computed for each trial (1000 trials in all) and, then, averaged. We also compute the standard deviation of the AE. Note that the AE is computed between the ground truth direction and the closest extracted ODF maxima until every maxima or ground truth direction are scanned. Hence, the DNC metric shows its importance since it gives information regarding the reliability of the AE. All the results are shown in Fig. 5.

Regarding the AE, we observe that the ℓ_1 recovery gives globally more accurate estimation of the directions than the ℓ_2 recovery. One explanation comes from the underlying property of the ℓ_1 recovery, which provides sharper ODF estimation, while the ℓ_2 constraint is known to favor low frequency components and thus provides smoother ODF estimation.

We, now, consider the DNC values of Fig. 5 (bottom curves). We observe, when a small number of samples is used, that the ℓ_2 recovery gives a more accurate DNC estimation than the ℓ_1 recovery. This observation is especially true when the SPF and the SPFdual bases are used to model the signal. Moreover, this phenomenon is emphasized for a small SNR. It may be due to the smoothing consequence of the ℓ_2 constraint, which somehow acts as a signal denoiser. However, this advantage of the ℓ_2 recovery is hampered by the very bad evaluation of the maxima directions extracted from the ODFs. For instance, at SNR = 10 and below $N = 30$, the AE exceeds 15°. Then, we cannot rely on the ℓ_2 recovery for diffusion directions evaluation while considering a small number of measurements in the reconstruction. To conclude on the DNC, only SHORE based ℓ_1 recovery is able to provide reliable ODF maxima, except for $N = 10$.

Overall, for a minimum of 20/30 measurements and above $SNR = 20$, SHORE based ℓ_1 recovery ensures reasonably low AE and DNC values, especially at SNR = 30, where the DNC is zero above $N = 30$ measurements. At SNR = 10 and above $N = 30$ measurements, we still have acceptable AE and DNC ($AE < 15°$ and $DNC < 0.5$) with the SHORE based ℓ_1 recovery. Then, we conclude that 20/30 measurements required are enough to obtain reliable and accurate diffusion directions from the estimated ODFs using the SHORE based ℓ_1 recovery (as concluded in Section 4.2.1).

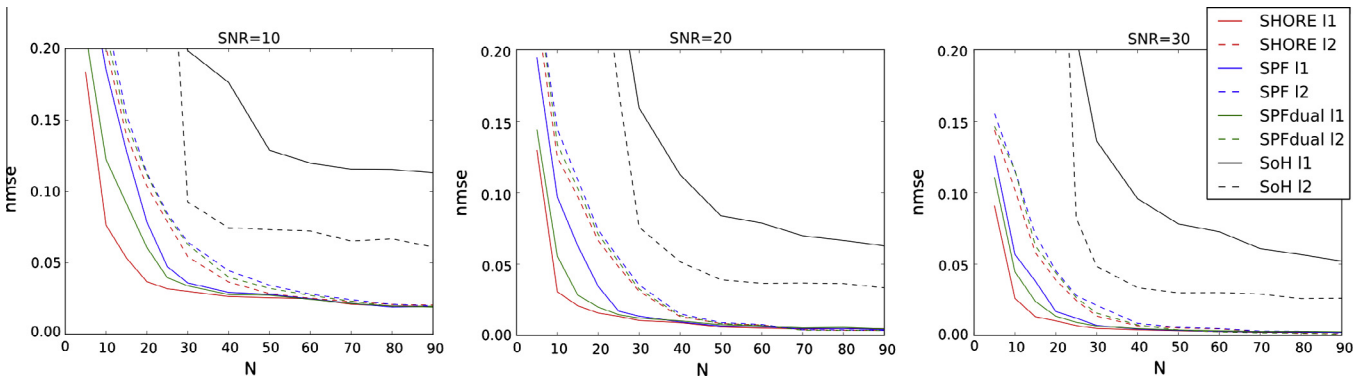

Fig. 4. NMSE for noisy and synthetic reconstruction with SNR = 10 to SNR = 30 (left to right). Results for ℓ_1 recovery is represented in plain line and results for ℓ_2 recovery is represented in dash line. We consider the SPF (in blue), SPFdual (in green), SoH (in black) and SHORE (in red) bases for the reconstruction. (For interpretation of the references to colour in this figure legend, the reader is referred to the web version of this article.)

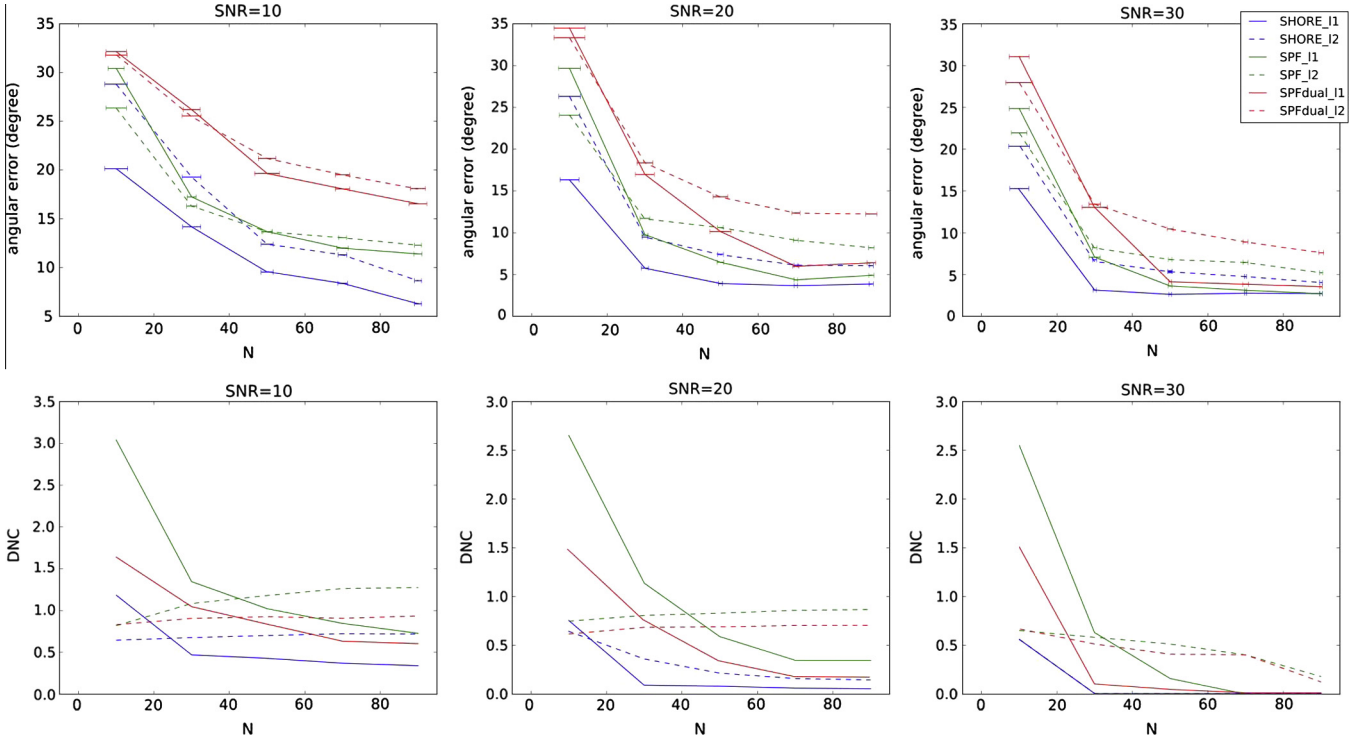

Fig. 5. Angular error (AE) and difference on the number of compartments (DNC) from noisy and synthetic ODF reconstruction with SNR = 10 to SNR = 30 (left to right). Results for ℓ_1 recovery are represented in plain line and results for ℓ_2 recovery are represented in dash line. We consider the SPF (in green), SPFdual (in red) and SHORE (in blue) bases for the reconstruction. (For interpretation of the references to colour in this figure legend, the reader is referred to the web version of this article.)

Finally, regarding the standard deviation of the error, we observe, as expected, an increase of these values for decreasing SNRs.

4.2.3. Comparison with DSI

Here, we compare the EAP estimated via a SHORE based ℓ_1 recovery and via the Diffusion Spectrum Imaging (DSI) technique (Wedeen et al., 2005).

We show quantitative results on the reconstruction of synthetic data, described in Appendix A. Again, we consider three cases: one fiber, two fibers crossing at 90° and two fibers crossing at 60°. Then, we generate the normalized diffusion signal E on a $11 \times 11 \times 11$ cartesian grid (1331 samples). The ground truth EAP P is the inverse Fourier Transform (IFT) of E. For DSI, we generate 514 DWIs in a cube plus an additional unweighted image. The number of 514 corresponds to the number of samples comprised within the sphere of five lattice unit radius. It is the common sampling protocol with the DSI technique. The EAP is, then, obtained by applying an hamming window and an inverse Fourier Transform. We choose the SHORE basis combined with ℓ_1 recovery for comparison. In this case, we reconstruct the diffusion signal for a number of samples $N = 10$–500. These samples are spread on three shells at b values $b = [1000, 2000, 3000]$ using the generalized Jones algorithm, where the radial distribution follow a law in q^1. Then, we use the closed form in Table 1 to estimate the EAP $\widetilde{P}$. For all the experiments, we add a Rician noise to the signal with $SNR = 20$. We evaluate the NMSE between $\widetilde{P}$ and the ground truth EAP P on the $11 \times 11 \times 11$ cartesian grid. For DSI this NMSE is fixed and equal to $NMSE_{DSI} = 0.025976$. For the SHORE based EAP reconstruction using the ℓ_1 recovery, we show in Fig. 6 the NMSE while taking $N = 10$–500 samples (blue curve). In the same figure, we plot a horizontal line (red line) whose the ordinate value is $NMSE_{DSI}$. We see in Fig. 6, that 180 measurements are necessary, with SHORE based ℓ_1 reconstruction, to attain the NMSE of DSI, which was obtained with 514 measurements plus an additional unweighted image. Therefore, an acceleration factor of $515/180 \sim 2.86$ is observed. Besides this improvement, our SHORE based ℓ_1 reconstruction has the advantage to give a continuous modeling of the EAP whereas the EAP based DSI reconstruction is dependent to the cartesian grid.

4.2.4. Conclusion on synthetic results

The conclusion to the noisy synthetic experiments is fourfold. First, these results show that the SHORE, SPF and SPFdual bases are appropriate for ℓ_1 recovery, and enables to reconstruct diffusion signals as accurately as with ℓ_2 recovery with a smaller number of measurements, whereas it is preferable to use an ℓ_2

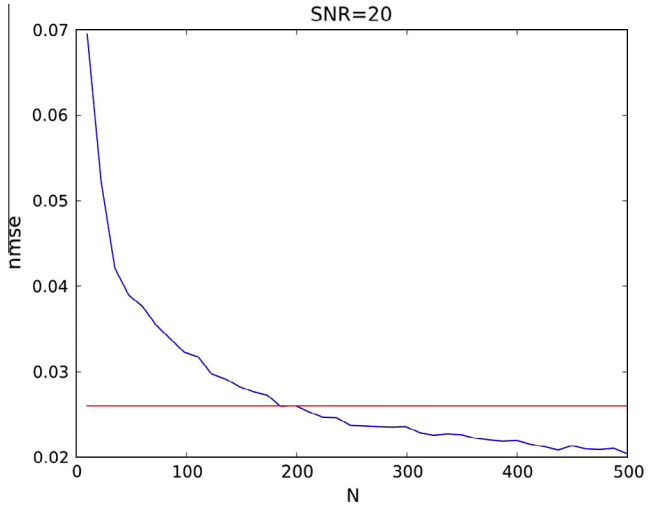

Fig. 6. Comparison between the NMSE obtained for DSI reconstruction (red line) and SHORE based ℓ_1 recovery (blue curve). (For interpretation of the references to colour in this figure legend, the reader is referred to the web version of this article.)

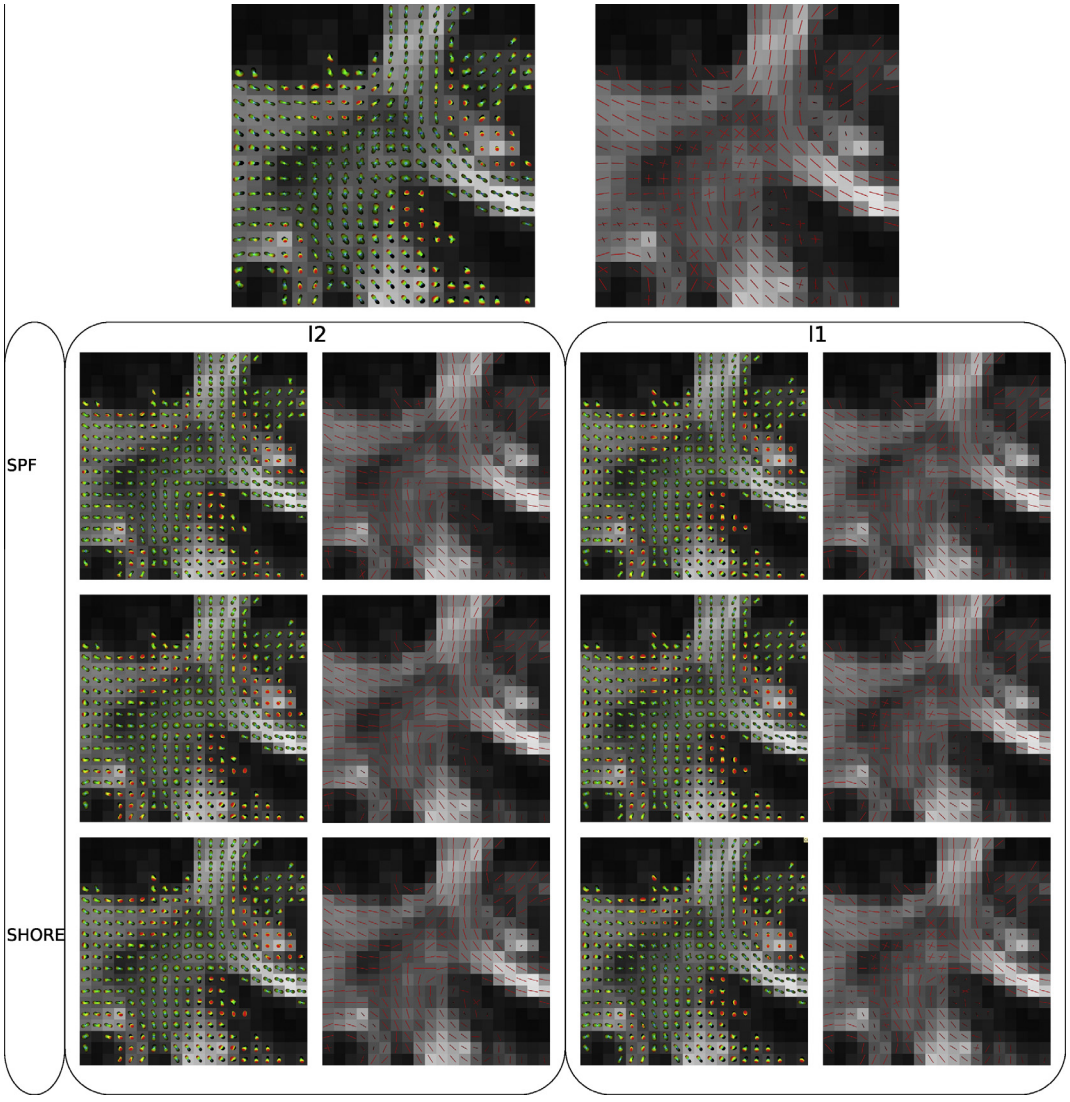

Fig. 7. ODF and extracted maxima. The underlying diffusion signal is estimated via ℓ_2 recovery (left part) and ℓ_1 recovery (right part). On the top is shown the ground truth of the region of interest. The array below shows the estimated ODF and extracted maxima. Three bases are used for the reconstruction: the Spherical Polar Fourier basis (Top line of the array), the Spherical Polar Fourier dual basis (Second line of the array), the Spherical Polar Fourier basis (Bottom line of the array).

recovery with the SoH basis. Next, we know that SHORE perfectly enter in the CS framework and is the most suitable basis to use for diffusion signal reconstruction via ℓ_1 recovery, where nearly 20/30 measurements are necessary to well estimate the diffusion signal. Then, considering the ODF experiments, we see that the SHORE based ℓ_1 recovery gives the best description of the angular information of the underlying synthetic signals. Overall, it provides lower DNC and AE values than the other reconstructions. In particular, we see that 30 measurements are sufficient to obtain a reliable and accurate estimation of the diffusion directions. Finally, we have performed a comparison with DSI and our experiments show that the association SHORE/ℓ_1 recovery enables to attain the accuracy of DSI with less than half the number of samples used in this high resolution acquisition technique (an acceleration factor of 2.86).

4.3. Real human brain data

We also performed experiments on a in vivo human brain. We acquired the data over 3 shells and 67 directions uniformly distributed on the sphere (A total of 201 directions). We used three b-values (500, 1000, and 2000 s mm^{-2}), and an imaging matrix of $93 \times 116 \times 93$ with isotropic voxels of 1.7 mm^3. The large number of samples enables to subsample the data and apply various sampling schemes. Based on our previous results, we take samples according to a radial distribution in q^1. All the experiments in this part are performed with 20 samples in both recovery methods (ℓ_1 and ℓ_2). The mean diffusivity constant averaged on all the voxels contained in the region of interest is $D = 0.00054$. We have $\tau = 0.0257$, then $\zeta = 925.93$ for SPF and SHORE bases, and $\zeta = 2.7357e{-}05$ (see Section 3.1 for details about ζ computation). We reconstruct the diffusion signal and, then, use the closed forms defined in Section 2 to compute the ODF. Fig. 7 shows the estimated ODFs and their extracted maxima while using SPF, SPFdual and SHORE in both ℓ_1 and ℓ_2 recovery methods. Regarding our previous experiments, we put aside the SoH basis. We put the fractional anisotropy in background of the region of interest. We also compute a ground truth by considering all the measurements. Because synthetic experiments show that every combination of basis and recovery method gives similar results when considering many measurements, we compute this near ground truth using the SHORE basis and the ℓ_2 recovery method.

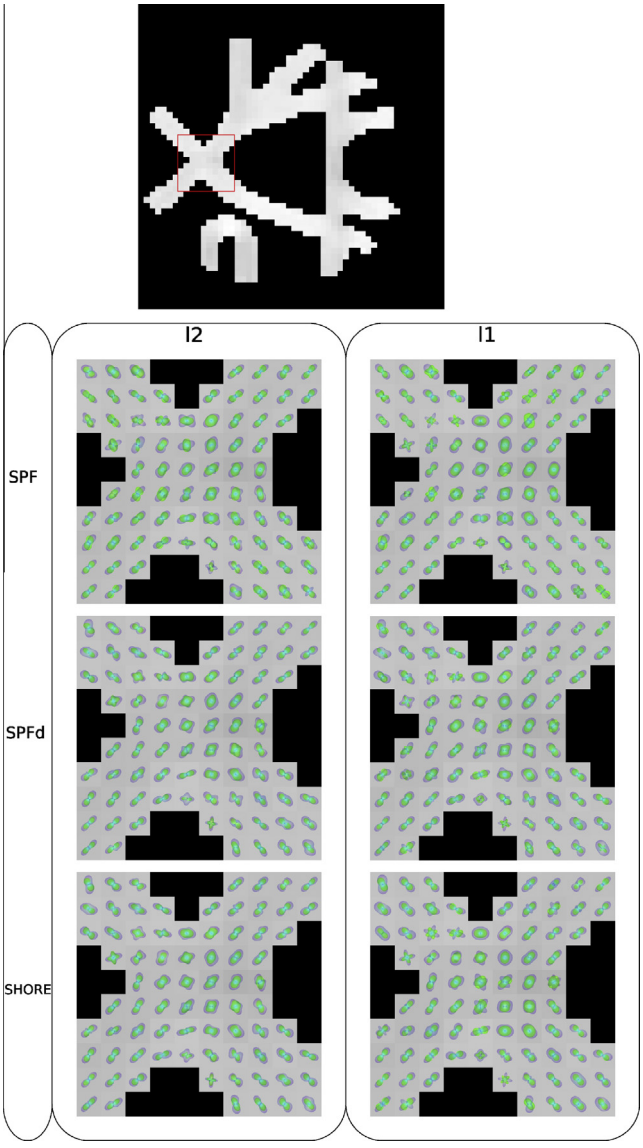

Fig. 8. Estimated EAP at radii 15 μm (green surface) and 20 μm (blue surface). The underlying diffusion signal is estimated via ℓ_2 recovery (left part) and CS recovery (right part). Three bases are used for the reconstruction: the Spherical Polar Fourier basis (top line), the Spherical Polar Fourier dual basis (second line), the Spherical Polar Fourier dual basis (bottom line). (For interpretation of the references to color in this figure legend, the reader is referred to the web version of this article.)

First at all, we focus our attention on the advantages/disadvantages of ℓ_1 over ℓ_2 recovery. We see that the ODF reconstructed using ℓ_1 recovery look sharper than in case of ℓ_2 recovery. This particularity is due to the nature of the ℓ_1 minimization problem. Indeed, the ℓ_1 regularization equally penalizes the low frequency components and the high frequency components, whereas the ℓ_2 regularization penalizes more the high frequency components. Hence, ℓ_1 recovery improves the angular resolution and produces sharper diffusion signal estimation than ℓ_2 recovery, and the ODFs appearance directly results from this phenomenon. This sharpening enables to extract more maxima. This was already observed from the synthetic experiments. With SPF and SPF dual bases, the CS based ODFs give also some maxima given by noisy peaks. ODFs estimated with SHORE basis and ℓ_1 recovery better agree the underlying structure and are not as perturbed as with SPF and SPFdual bases. Then, SHORE basis better resolves the crossing area using ℓ_1 recovery and 20 measurements without catching as much noise.

In conclusion, SHORE appears to be the best basis, which especially gives good results in case of ℓ_1 recovery with only 20 samples. Overall, ℓ_1 recovery gives sharper ODF than ℓ_2 recovery.

4.4. Phantom data

Here, we perform our experiments on a phantom data provided by LNAO, which was used in a fiber cup contest in MICCAI 2009 (Poupon et al., 2008; Fillard et al., 2011). Diffusion-weighted data of the phantoms were acquired at a spatial resolution of 3 mm^3 isotropic and an imaging matrix of $64 \times 64 \times 3$. The data were obtained for three different b-values $b = 650/1500/2000$ s mm^{-2} along a set of 64 orientations, uniformly distributed over the sphere (A total of 192 directions).

In this experiment, we consider a crossing region and estimate the diffusion signal in three bases: SPF, SPFdual and SHORE. Again, we put aside the SoH basis and take only 20 samples. The mean diffusivity constant averaged on the crossing region is $D = 0.00081$. We have $\tau = 0.0253$, then $\zeta = 617.28$ for SPF and SHORE bases, and $\zeta = 4.1035e{-}05$ for SPFdual basis (see Section 3.1 for details about ζ computation). Fig. 8 shows the EAP at radii 15 μm and 20 μm.

We analytically compute the EAP from the closed formula described in Section 2. Again, the EAPs estimated with ℓ_1 recovery are sharper that the EAPs estimated with ℓ_2 recovery Based on the known ground truth, we can say that our best estimation are again the one based on the association ℓ_1 recovery/SHORE basis,

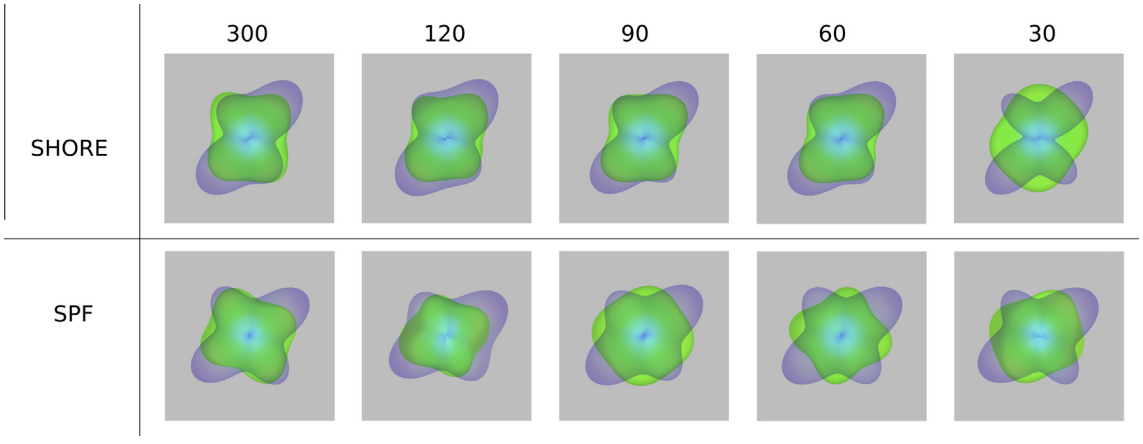

Fig. 9. Estimated EAP at radii 15 μm (green surface) and 20 μm (blue surface) for different number of samples, while the diffusion signal is modeled with SHORE and SPF bases (respectively top and bottom lines). We used $N = 300$, $N = 120$, $N = 90$, $N = 60$, $N = 30$ samples (from left to right) for the reconstruction. (For interpretation of the references to colour in this figure legend, the reader is referred to the web version of this article.)

because its EAP estimation agrees more the underlying crossing area than the other estimations.

In Fig. 9, we compare estimated EAP modeled with SPF and SHORE bases for different numbers of samples. For this purpose, we take a voxel in the phantom where fibers are crossing. We set a 'pseudo' ground truth (GT) as the reconstructed signal for both bases using the whole set of acquisitions ($N = 300$ samples). Then, we estimate the EAP at radii 15 μm (green surface) and 20 μm (blue surface) and show it in Fig. 9 (first column). Afterward, we repeat the experiment for $N = 120$, $N = 90$, $N = 60$, $N = 30$ samples. Considering SHORE basis, we note that the estimated EAP is qualitatively similar to the 'pseudo' GT for both radii from $N = 120$ to $N = 60$. For a smaller N the angular information at radius 15 μm becomes too smooth to correctly estimate the diffusion directions. For SPF basis, we remark that this phenomenon (the bad estimation of the diffusion directions at a low radius) appears at $N = 90$. Indeed, at radius 15 μm the diffusion directions given are staggered with the ground truth. On the whole, we see a better angular resolution for higher radii.

This example shows the efficiency of SHORE basis to correctly model the signal (and so the EAP) with less samples than needed with the SPF basis. These remarks hold for a ℓ_1 recovery scheme.

5. Conclusion

We have proposed a new solution to characterize the complete water diffusion process in the white matter, with a very small number of measurements (only 20/30 measurements). The main contribution of this paper is the investigation of Compressive Sensing to estimate the whole 3D diffusion signal in diffusion MRI. We reviewed every point of CS both in a theoretical and experimental ways for the dMRI purpose. We showed the importance of the sparsity, the incoherence and the RIP in estimating the diffusion signal using an ℓ_1 minimization scheme. Moreover, in this approach, we considered only continuous frameworks, which enable to compute analytical solutions of the EAP and ODF. The EAP captures both radial and angular information and completely describes the diffusion process. The ODF is the diffusion feature commonly used to perform tractography. Derivation of more features seems conceivable in these frameworks.

Our extensive review of CS for modeling the diffusion signal using SPF, SPFdual, SoH and SHORE bases leads to two important conclusions about: (1) the efficiency of a ℓ_1 recovery compared to a ℓ_2 recovery and (2) the conditions for an efficient CS recovery. At first, why should we use a ℓ_1 recovery rather than a ℓ_2 recovery? We showed, when the CS requirements are fulfilled, that a ℓ_1 recovery produces better diffusion signal estimation than the ℓ_2 recovery method does, with not more than 20/30 samples optimally spread. Moreover, ODFs estimated from a ℓ_1 recovery are sharper than with a ℓ_2 recovery and, thus, could be efficiently used for tractography. Nevertheless, we found that the CS technique is quite constrained. Even if we can fully choose our samples to nearly respect the RIP property, two other conditions depend directly on the signal to recover and the basis used for modeling it. These conditions, the sparsity and the incoherence, are not fulfilled for every case. For instance, the SoH basis is not theoretically appropriate for the CS technique. Inversely, the theory pointed out the efficiency of SHORE basis in CS recovery, which was confirmed by experimental results.

To conclude, we showed that the Compressive Sensing technique enables to accurately estimate the diffusion signal along with the EAP and the ODF with only 20/30 samples. However, the Compressive Sensing theory is not easy to handle and is more appropriate, in some cases, than the commonly used ℓ_2 recovery method. In this investigation, we also found an adequate association which fulfills the CS requirements. High sparsity and incoherence are given by SHORE basis and the RIP property is approximately satisfied with a robust multiple shells sampling protocol, which is performed by the generalized Jones algorithm by setting a number of samples by shells proportional to q^1. Moreover, we get rid of the problem of sensitivity towards the regularization parameter in ℓ_1 recovery by using cross validation.

To resume, we showed that CS Diffusion MRI holds great promise for reconstructing the full water diffusion process within a clinically feasible acquisition time. This opens new and exciting perspectives in diffusion MRI.

Appendix A. Analytical diffusion signal, propagator and ODF from the multiple tensor model

We assume the normalized diffusion signal $E(\mathbf{q})$ is generated from the multi-tensor model for n fibers

$$E(q\mathbf{u}) = \sum_{f=1}^{F} p_f \exp(-4\pi^2\tau q^2 \mathbf{u}^T D_f \mathbf{u}), \tag{A.1}$$

where a fibre f is defined by a tensor matrix D_f and weight p_f. q denotes the norm of the effective gradient and $\mathbf{u}$ is a unitary vector in Cartesian coordinate.

The analytical ground truth of the EAP for any radius R is then given by

$$P(R\mathbf{r}) = \sum_{f=1}^{F} p_f \frac{1}{\sqrt{(4\pi\tau)^3 |D_f|}} \exp\left(\frac{-R^2 \mathbf{r}^T D_f^{-1} \mathbf{r}}{4\tau}\right), \tag{A.2}$$

with $\mathbf{r}$ a unitary vector in Cartesian coordinate.

We can also check the ODF feature using solid angle closed form expression (Aganj et al., 2010; Tristn-Vega et al., 2009),

$$\psi(r) = \sum_{f=1}^{F} p_f \frac{1}{4\pi |D_f|^{\frac{1}{2}} \left(\mathbf{r}^T D_f^{-1} \mathbf{r}\right)^{\frac{3}{2}}}. \tag{A.3}$$

Appendix B. Proof of the analytical ODF solution when the signal is modeled in SPF dual basis

In the SPF formalism, one can express the ODF as,

$$\begin{aligned}\Upsilon(\mathbf{r}) &= \int_{R=0}^{\infty} \sum_{n=0}^{N} \sum_{\ell=0}^{L} \sum_{m=-\ell}^{\ell} c_{nlm} K_n(R) Y_\ell^m(\mathbf{r}) R^2 \, dR \\ &= \sum_{\ell=0}^{L} \sum_{m=-\ell}^{\ell} Y_\ell^m((\mathbf{r})) \underbrace{\sum_{n=0}^{N} c_{nlm} \int_{R=0}^{\infty} K_n(R) R^2 \, dR}_{\upsilon_{\ell m}}.\end{aligned}$$

$$\text{with } K_n(R) = \left[\frac{2n!}{\zeta^{3/2}\Gamma(n+3/2)}\right]^{1/2} exp\left(\frac{-R^2}{2\zeta}\right) L_n^{1/2}\left(\frac{R^2}{\zeta}\right). \tag{B.1}$$

Using the formula $\int_0^\infty exp(-sx) x^\alpha L_n^\alpha(x) dx = \frac{\Gamma(\alpha+n+1)(s-1)^n}{n! s^{\alpha+n+1}}$ (Ryzhik et al., 2007) and this substitution: $R = \sqrt{x\zeta}$ and $dR = \frac{1}{2}\sqrt{\frac{\zeta}{x}} dx$, we get

$$\begin{aligned}\upsilon_{\ell m} &= \sum_{n=0}^{N} c_{nlm} \frac{\zeta^{3/2}}{2} \left[\frac{2n!}{\zeta^{3/2}\Gamma\left(n+\frac{3}{2}\right)}\right]^{1/2} \frac{\Gamma\left(\frac{3}{2}+n\right)\left(-\frac{1}{2}\right)^n}{n!\frac{1}{2}^{(3/2+n)}} \\ &= \sum_{n=0}^{N} c_{nlm} 2(-1)^n \zeta^{3/4} \left[\frac{\Gamma\left(n+\frac{3}{2}\right)}{n!}\right]^{1/2}\end{aligned} \tag{B.2}$$

Appendix C. Proof of the analytical ODF solution when the signal is modeled in SHORE basis

In the SHORE formalism, one can express the ODF as,

$$\Upsilon(\mathbf{r}) = \int_{R=0}^{\infty} \sum_{n=0}^{N} \sum_{\ell=0}^{L} \sum_{m=-\ell}^{\ell} c_{nlm} K_n(R) Y_\ell^m(\mathbf{r}) R^2 \, dR$$
$$= \sum_{\ell=0}^{L} \sum_{m=-\ell}^{\ell} Y_\ell^m((\mathbf{r})) \underbrace{\sum_{n=0}^{N} c_{nlm} \int_{R=0}^{\infty} K_n(R) R^2 \, dR}_{\upsilon_{\ell m}}$$

$$\text{with } K_n(R) = (-1)^{n-l/2} \left[\frac{2(4\pi^2\zeta)^{3/2}(n-\ell)!}{\Gamma(n+3/2)} \right]^{1/2} \left(4\pi^2\zeta R^2\right)^{l/2}$$
$$\times \exp\left(-2\pi^2\zeta R^2\right) L_{n-l}^{l+1/2}(4\pi^2\zeta R^2) \tag{C.1}$$

Using the formula $\int_0^\infty exp(-sx) x^\beta L_n^\alpha(x) dx = \frac{\Gamma(\beta+1)\Gamma(\alpha+n+1)}{n!\Gamma(\alpha+1)} s^{-\beta-1}{}_2F_1(-n, \beta+1; \alpha+1, 1/s)$ (Ryzhik et al., 2007) and this substitution: $R = \sqrt{\frac{x}{4\pi^2\zeta}}$ and $dR = \frac{1}{2}\sqrt{\frac{1}{4\pi^2\zeta x}} dx$, we get

$$\upsilon_{\ell m} = \sum_{n=0}^{N} c_{n\ell m} \frac{(-1)^{n-l/2}}{2(4\pi^2\zeta)^{3/2}} \left[\frac{2(4\pi^2\zeta)^{3/2}(n-l)!}{\Gamma(n+3/2)} \right]^{1/2} \tag{C.2}$$
$$\frac{\Gamma(\ell/2+3/2)\Gamma(3/2+n)}{\Gamma(l+3/2)(n-l)!} \left(\frac{1}{2}\right)^{-\ell/2-3/2} \tag{C.3}$$
$${}_2F_1(-n+l, l/2+3/2; l+3/2; 2) \tag{C.4}$$

References

Aganj, I., Lenglet, C., Sapiro, G., Yacoub, E., Ugurbil, K., Harel, N., 2010. Reconstruction of the orientation distribution function in single- and multiple-shell q-ball imaging within constant solid angle. Magnetic Resonance in Medicine 64, 554–566.

Anderson, A.W., 2005. Measurement of fiber orientation distributions using high angular resolution diffusion imaging. Magnetic Resonance in Medicine 54, 1194–1206.

Assemlal, H., Tschumperlé, D., Brun, L., 2009. Efficient and robust computation of pdf features from diffusion MR signal. Medical Image Analysis 13, 715–729.

Basser, P.J., Mattiello, J., Le Bihan, D., 1994a. Estimation of the effective self-diffusion tensor from the NMR spin echo. Journal of Magnetic Resonance, Series B 103, 247–254.

Basser, P.J., Mattiello, J., Le Bihan, D., 1994b. Mr diffusion tensor spectroscopy and imaging. Biophysical Journal 66, 259–267.

Beck, A., Teboulle, M., 2009. A fast iterative shrinkage-thresholding algorithm for linear inverse problems. SIAM Journal on Imaging Sciences 2, 183–202, <http://epubs.siam.org/doi/pdf/10.1137/080716542>.

Bilgic, B., Setsompop, K., Cohen-Adad, J., Yendiki, A., Wald, L.L., Adalsteinsson, E., 2012. Accelerated diffusion spectrum imaging with compressed sensing using adaptive dictionaries. Magnetic Resonance in Medicine 68, 1747–1754.

Candès, E., 2008. The restricted isometry property and its implications for compressed sensing. Comptes Rendus Mathematique 346, 589–592.

Candes, E., Plan, Y., 2011. A probabilistic and RIPless theory of compressed sensing. IEEE Transactions on Information Theory 57, 7235–7254.

Candes, E., Wakin, M., 2008. An introduction to compressive sampling. IEEE Signal Processing Magazine 25, 21–30.

Cands, E., Romberg, J., 2007. Sparsity and incoherence in compressive sampling. Inverse Problems 23, 969.

Cands, E.J., Eldar, Y.C., Needell, D., Randall, P., 2011. Compressed sensing with coherent and redundant dictionaries. Applied and Computational Harmonic Analysis 31, 59–73.

Caruyer, E., Cheng, J., Lenglet, C., Sapiro, G., Jiang, T., Deriche, R., 2011a. Optimal design of multiple q-shells experiments for diffusion MRI. In: MICCAI Workshop on Computational Diffusion MRI – CDMRI'11, Toronto, Canada.

Caruyer, E., Lenglet, C., Sapiro, G., Deriche, R., 2011b. Incremental gradient table for multiple q-shells diffusion MRI. In: HBM 17th Annual Meeting, Quebec, Canada.

Chartrand, R., 2009. Fast algorithms for nonconvex compressive sensing: MRI reconstruction from very few data.

Cheng, J., Ghosh, A., Deriche, R., Jiang, T., 2010a. Model-free, regularized, fast, and robust analytical orientation distribution function estimation. In: Medical Image Computing and Computer-Assisted Intervention – MICCAI. Springer, pp. 648–656.

Cheng, J., Ghosh, A., Jiang, T., Deriche, R., 2010b. Model-free and analytical EAP reconstruction via spherical polar fourier diffusion MRI. In: Medical Image Computing and Computer-Assisted Intervention – MICCAI, pp. 590–597.

Cheng, J., Jiang, T., Deriche, R., 2011a. Theoretical analysis and practical insights on EAP estimation via a unified HARDI framework. In: MICCAI workshop on Computational Diffusion MRI.

Cheng, J., Merlet, S., Caruyer, E., Ghosh, A., Jiang, T., Deriche, R., 2011b. Compressive sensing ensemble average propagator estimation via l1 spherical polar fourier imaging. In: MICCAI Workshop on Computational Diffusion MRI.

Cook, P.A., Bai, Y., Nedjati-Gilani, S., Seunarine, K.K., Hall, M.G., Parker, G.J., Alexander, D.C., 2006. Camino: Open-source diffusion-MRI reconstruction and processing. In: 14th ISMRM, Seattle, USA.

Craven, P., Wahba, G., 1985. Smoothing noisy data with spline functions. Numerische Mathematik 31, 377–403.

Deriche, R., Calder, J., Descoteaux, M., 2009. Optimal real-time q-ball imaging using regularized Kalman filtering with incremental orientation sets. Medical Image Analysis 13, 564–579.

Descoteaux, M., Angelino, E., Fitzgibbons, S., Deriche, R., 2007. Regularized, fast, and robust analytical q-ball imaging. Magnetic Resonance in Medicine 58, 497–510.

Descoteaux, M., Deriche, R., Le Bihan, D., Mangin, J.F., Poupon, C., 2011. Multiple q-shell diffusion propagator imaging. Medical Image Analysis 15, 603–621.

Donoho, D., 2006. Compressed sensing. IEEE Transactions on Information Theory 52, 1289–1306.

Donoho, D., 2010. Method and apparatus for compressed sensing. US Patent 7 (646), 924.

Fillard, P., Descoteaux, M., Goh, A., Gouttard, S., Jeurissen, B., Malcolm, J., Ramirez-Manzanares, A., Reisert, M., Sakaie, K., Tensaouti, F., Yo, T., Mangin, J.F., Poupon, C., 2011. Quantitative evaluation of 10 tractography algorithms on a realistic diffusion mr phantom. NeuroImage 56, 220–234.

Ganesh, A., Edward, V. R. D., Reordering for Improved Constrained Reconstruction from Undersampled k-Space Data, International Journal of Biomedical Imaging 2008, pp.12, http://dx.doi.org/10.1155/2008/341684.

Gramfort, A., Poupon, C., Descoteaux, M., 2012. Sparse DSI: Learning DSI Structure for Denoising and Fast Imaging. Springer (pp. 288–296).

Guo, W., Yin, W., 2010. Edgecs: Edge guided compressive sensing reconstruction. Rice CAAM Report TR10 2, p. 30.

Hosseinbor, A., Chung, M., Wu, Y.C., Alexander, A., 2011. Bessel fourier orientation reconstruction: an analytical EAP reconstruction using multiple shell acquisitions in diffusion MRI. In: Fichtinger, G., Martel, A., Peters, T. (Eds.), Medical Image Computing and Computer-Assisted Intervention – MICCAI 2011. Springer, Berlin/Heidelberg, pp. 217–225.

Jian, B., Vemuri, B.C., zarslan, E., Carney, P.R., Mareci, T.H., 2007. A novel tensor distribution model for the diffusion-weighted MR signal. NeuroImage 37, 164–176.

Jones, D., Horsfield, M., Simmons, A., 1999. Optimal strategies for measuring diffusion in anisotropic systems by magnetic resonance imaging. Magnetic Resonance in Medicine 42, 515–525.

Le Bihan, D., Breton, E., 1985. Imagerie de diffusion in vivo par résonnance magnétique nucléaire. CR Académie des Sciences, 1109–1112.

Lustig, M., Donoho, D., Pauly, J.M., 2007. Sparse MRI: the application of compressed sensing for rapid mr imaging. Magnetic Resonance in Medicine 58, 1182–1195.

Menzel, M.I., Tan, E.T., Khare, K., Sperl, J.I., King, K.F., Tao, X., Hardy, C.J., Marinelli, L., 2011. Accelerated diffusion spectrum imaging in the human brain using compressed sensing. Magnetic Resonance in Medicine 66, 1226–1233.

Merboldt, K.D., Hanicke, W., Frahm, J., 1985. Self-diffusion nmr imaging using stimulated echoes. Journal of Magnetic Resonance 64 (1969), 479–486.

Merlet, S., Deriche, R., 2010. Compressed sensing for accelerated EAP recovery in diffusion MRI. In: Proceedings Computational Diffusion MRI – MICCAI Workshop.

Merlet, S., Caruyer, E., Deriche, R., 2011a. Impact of radial and angular sampling on multiple shells acquisition in diffusion MRI. In: MICCAI. Springer, pp. 113–121.

Merlet, S., Cheng, J., Ghosh, A., Deriche, R., 2011b. Spherical polar fourier EAP and ODF reconstruction via compressed sensing in diffusion MRI. In: Proceedings of ISBI.

Merlet, S., Caruyer, E., Deriche, R., 2012. Parametric Dictionary Learning for Modeling EAP and ODF in Diffusion MRI. Springer (pp. 10–17).

Michailovich, O., Rathi, Y., 2010. On approximation of orientation distributions by means of spherical ridgelets. IEEE Transactions on Image Processing 19, 461–477.

Ozarslan, E., Koay, C., Shepherd, T., Blackband, S., Basser, P., 2009. Simple harmonic oscillator based reconstruction and estimation for three-dimensional q-space MRI. In: ISMRM 17th Annual Meeting and Exhibition, Honolulu, pp. 1396.

Poupon, C., Rieul, B., Kezele, I., Perrin, M., Poupon, F., Mangin, J.F., 2008. New diffusion phantoms dedicated to the study and validation of high-angular-resolution diffusion imaging (HARDI) models. Magnetic Resonance in Medicine 60, 1276–1283.

Rathi, Y., Michailovich, O., Setsompop, K., Bouix, S., Shenton, M., Westin, C., 2011. Sparse multi-shell diffusion imaging. In: MICCAI. Springer, pp. 58–65.

Ryzhik, I., Jeffrey, A., Zwillinger, D., 2007. Table of Integrals, Series and Products. Academic Press.

Saint-Amant, E., Descoteaux, M., 2011. Sparsity characterization of the diffusion propagator, in: Proceedings of ISMRM.

Stejskal, E.O., Tanner, J.E., 1965. Spin diffusion measurements: Spin echoes in the presence of a time-dependent field gradient. The Journal of Chemical Physics 42, 288–292.

Taylor, D., Bushell, M., 1985. The spatial mapping of translational diffusion coefficients by the nmr imaging technique. Physics in Medicine and Biology 30, 345–349.

Tristán-Vega, A., Westin, C.F., 2011. n-Vega and Westin (2011). Probabilistic ODF estimation from reduced HARDI data with sparse regularization. Medical Image Computing and Computer-Assisted Intervention-MICCAI, pp. 182–190.

Tristn-Vega, A., Westin, C.F., Aja-Fernndez, S., 2009. Estimation of fiber orientation probability density functions in high angular resolution diffusion imaging. NeuroImage 47, 638–650.

Tuch, D.S., 2004. Q-ball imaging. Magnetic Resonance in Medicine 52, 1358–1372.

Ward, R., 2009. Compressed sensing with cross validation. IEEE Transactions on Information Theory 55, 5773–5782.

Wedeen, V.J., Hagmann, P., Tseng, W.Y.I., Reese, T.G., Weisskoff, R.M., 2005. Mapping complex tissue architecture with diffusion spectrum magnetic resonance imaging. Magnetic Resonance in Medicine 54, 1377–1386.

Wu, Y.C., Alexander, A.L., 2007. Hybrid diffusion imaging. NeuroImage 36, 617–629.

Ye, W., Vemuri, B., Entezari, A., 2012. An over-complete dictionary based regularized reconstruction of a field of ensemble average propagators. In: 2012 9th IEEE International Symposium on Biomedical Imaging (ISBI). IEEE, pp. 940–943.

zarslan, E., Shepherd, T.M., Vemuri, B.C., Blackband, S.J., Mareci, T.H., 2006. Resolution of complex tissue microarchitecture using the diffusion orientation transform (dot). NeuroImage 31, 1086–1103.

Zibulevsky, M., Elad, M., 2010. L1-l2 optimization in signal and image processing. IEEE Signal Processing Magazine 27, 76–88.